Clonal Hematopoiesis Associated with *TP53* and *DNMT3A* Mutations Promotes Tissue Repair in Acute Cardiovascular Diseases

Yi Pan*[1,2], XiaDuo Meng[1,2], Chen Wang[1,2], WenXuan Zhou[1,2], Qin Zhou[1,5,8,9], Jingshu Chi[10], Breton Barrier[4], Luis Martinez-Lemus[1,6,7], De-Pei Li[1,5], Zhenguo Liu[10], XunLei Kang*[1,2,3]

1 Center for Precision Medicine, Department of Medicine, University of Missouri School of Medicine, Columbia, MO 65212, USA

2 Ellis Fischel Cancer Center at MU Health Care, University of Missouri, Columbia, MO 65212, USA

3 Division of Hematology and Oncology, Department of Medicine, University of Missouri School of Medicine, Columbia, MO 65212, USA

4 Department of Obstetrics & Gynecology and Women's Health, University of Missouri School of Medicine, Columbia, MO 65212, USA

5 Division of Cardiovascular Medicine, Department of Medicine, University of Missouri School of Medicine, Columbia, MO 65212, USA,

6 Dalton Cardiovascular Research Center, University of Missouri, Columbia, Missouri

7 Department of Medical Pharmacology and Physiology, University of Missouri School of Medicine, Columbia, Missouri

8 Department of Clinical Laboratory, Chengdu Women's and Children's Central Hospital, Chengdu 610091, PR China

9 Department of Cardiology, Children's Hospital of Chongqing Medical University, Chongqing, 400014, P.R. China.

10 Internal Medicine Cardiovascular medicine, University of Nebraska Medical Center. Omaha,NE 68106

*Correspondence: X.K.: kangxu@health.missouri.edu; Y.P.: ypvcm@missouri.edu

Abstract

Clonal hematopoiesis (CH), arising from hematopoietic progenitor cells with acquired mutations, resulting in clonal expansion, and displaying functionally altered hematopoietic cells, is traditionally associated with adverse health outcomes of numerous conditions. However, CH may not always be pathological - our study found that CH associated with *DNMT3A* and *TP53* promotes tissue regeneration after acute injury, indicating the positive effects of CH. Genetics analysis of 125,966 patients revealed that individuals with *TET2* and *JAK2* CH show worse prognosis in acute cardiovascular diseases, while no significant association was observed among individuals with *DNMT3A* and *TP53* mutations. In mouse models of myocardial infarction, hindlimb ischemia, and muscle injury, we utilized competitive bone marrow transplantation to mimic CH with *Dnmt3a* and *Trp53* mutations. Mice with CH demonstrated enhanced tissue repair compared to controls. Single-cell RNA sequencing of recovering tissues and residing hematopoietic cells indicated that clonal hematopoiesis was associated with the presence of diverse hematopoietic cell populations exhibiting pro-regenerative functions. Notably, macrophages from CH mice showed increased expression of VEGF, contributing to improved tissue repair. Signaling analysis showed that suppressed E2F family transcription factors drive higher expression of *Vegfa*. These results suggest that CH may play a role in promoting recovery following ischemic injury and highlight its potential as a therapeutic strategy for improving outcomes in ischemic disease.

Introduction

Clonal hematopoiesis (CH) occurs when specific mutations arise in hematopoietic stem cells (HSCs), leading to the clonal expansion of the mutated population[1,2]. Mutations frequently associated with CH, such as *DNMT3A*, *TET2*, and *TP53*, have been shown to alter the function and differentiation of hematopoietic cells, thereby affecting other organ systems[3,4]. Traditionally, CH has been linked to adverse outcomes and is recognized as a risk factor for various conditions, including myeloid malignancies, cardiovascular disorders, periodontal disease, osteoporosis, and gout[3,5-8]. Among cardiovascular diseases (CVDs), CH is a well-accepted risk factor for its development[9,10] as well as a driver for worse clinical outcomes[5,11]. However,

previous studies assessed outcomes in individuals with chronic CVDs, such as arteriosclerosis and heart failures[12-14], or pooled both chronic and acute CVDs[12], while the association between CH and acute CVDs is not well-explored.

Acute CVDs often involve ischemic events, such as myocardial infarction (MI) and critical limb ischemia, and remain the leading causes of morbidity and mortality, particularly among elderly populations[15]. While CH increases the risks for MI[10], it does not appear to elevate the risk of MI recurrence[16], suggesting a more complex role of CH in MI. In contrast, the potential involvement of CH in critical limb ischemia remains unexplored.

In the context of MI, *Tet2* mutations have been directly linked to worse outcomes and impaired tissue regeneration in mouse models[17]. However, the impact of CH driven by other mutations, such as *DNMT3A* and *TP53*, remains understudied, underscoring a critical gap in our understanding of CH's broader implications in acute CVDs.

Results

Clonal Expansion Driven by *Trp53* and *Dnmt3a* Mutations

To test our hypothesis, we mimicked *DNMT3A*- and *TP53*-CH in mice and tested their association with three acute CVD mouse models – MI, hindlimb ischemia (HLI), and cardiotoxin-induced muscle damage. To model CH in a controlled experimental setting and assess its impact on post-ischemia regeneration, we employed a competitive bone marrow transplantation (BMT) approach to generate chimeric mice. These mice carried a small proportion of hematopoietic stem and progenitor cells (HSPCs) with either the *Trp53*$^{R172H/+}$ (derived from *Trp53*$^{R172H\text{-}wm}$; Scl-CreER^{T} mice) or *Dnmt3a*$^{R878H/+}$ (derived from *Dnmt3a*$^{fl\text{-}878H}$; Scl-CreER^{T} mice) mutations[18]. Lethally irradiated C57/B6 recipients were transplanted with bone marrow (BM) cell suspensions consisting of 10% mutant (*Trp53*$^{R172H/+}$, or *Dnmt3a*$^{R878H/+}$) cells mixed with 90% wild-type (WT) cells (**Fig. 1A**). To distinguish between donor mutant and WT cells, the *Trp53*$^{R172H/+}$ or *Dnmt3a*$^{R878H/+}$ cells were derived from mice expressing the CD45.2 variant, while WT cells were obtained from CD45.1^{+} mice (*Trp53* or *Dnmt3a* CH mice). Control mice received 10% CD45.2^{+} WT cells and 90% CD45.1^{+} WT cells (Ctrl mice). Thirteen weeks post-transplantation, flow cytometry of CD45.2^{+} cells confirmed successful clonal expansion of mutant hematopoietic cells to levels consistent with those observed in human CH (**Fig. 1B-C**)[1]. Mice were then subjected to injury to evaluate tissue repair in CH and Ctrl mouse models.

CH Enhances Cardiac Repair After MI

We first evaluated whether CH enhances cardiac repair following MI. Adult mice were subjected to permanent ligation of the left anterior descending artery (LAD). Remarkably, CH mice exhibited improved cardiac function post-MI, as evidenced by higher left ventricular ejection fraction and preserved wall thickness (**Fig. 2A to B; Fig. S1A**). Histological analysis revealed reduced scar formation in CH mice, with significant reductions observed by day 14 post-injury (**Fig. 2C to D; Fig. S1B**). Furthermore, CH mice demonstrated increased cardiomyocyte cell-cycle re-entry, as indicated by elevated Ki67 and AuroraB expression in the myocardium adjacent to the infarcted region (**Fig. 2E**). Notably, these improvements were accompanied by increased presence of endothelial cells in the myocardium (**Fig. 2F; Fig. S1C**), suggesting a pro-angiogenic effect.

CH Promotes Vascular Regeneration After HLI

To further explore the regenerative and pro-angiogenic potential of CH, we subjected mice to a vascular injury model (HLI) by femoral artery ligation (FAL). Blood flow recovery in the ischemic limb, compared to the contralateral control limb, was assessed at various time points. The initial reduction in blood flow ratio was not different between CH and control mice. However, CH mice exhibited significantly faster and more complete recovery of blood flow compared to control mice over the same time period (**Fig. 3A; Fig. S1D**). Corresponding to improved blood flow and limb function, CH mice also demonstrated higher capillary density by day 21 (2.7-fold increase in *Trp53* CH mice and 2.4-fold increase in *Dnmt3a* CH mice at day 7; 3.3-fold and 2.9-fold increases, respectively, at day 21; calculated by ($density_{CH}$ - $density_{Ctrl}$)/$density_{Ctrl}$) (**Fig. 3B; Fig. S1E**)[19]. Additionally, CH mice exhibited not only increased numbers of arterioles but also significantly larger arterioles compared to controls (**Fig. 3C; Fig. S1F**).

CH Accelerates Muscle Regeneration in Ischemic and Non-Ischemic Models

Beyond vascular regeneration, CH mice displayed enhanced muscle regeneration and reduced necrosis in the HLI model (**Fig. 4A and B**). However, the peak of CH mice necrosis is significantly lower than that in the Ctrl mice (**Fig. 4A**), indicating CH mice may have either higher resistance to muscle necrosis or faster resolution of necrotic tissue. In addition, it is unclear whether the accelerated muscle regeneration was dependent on vascular repair or could occur independently. To investigate this, we used a cardiotoxin (CTX) injury model, which induces rapid muscle damage without affecting the vasculature[20]. After CTX injection, CH mice showed similar peaks but quicker resolution of muscle necrosis (**Fig. 4C and D; Fig. S1G**) and earlier regeneration of myofibers (**Fig. 4E; Fig. S1H**). Consistently, both models demonstrated reduced muscle cell death quantified by Caspase-3 in CH mice (**Fig. 4F to G; Fig. S1J**). Seven days after CTX injection or 14 days post-FAL, CH mice exhibited fewer early-regenerating myofibers (eMyHC$^+$) and more late-regenerating myofibers (eMyHC$^-$) compared to controls, indicating faster muscle regeneration (**Fig. 4H; Fig. S1K**). CH mice also showed more rapid proliferation and differentiation of satellite cells, as assessed by pH3, Pax7, and Myog, essential for muscle repair[21,22] (**Fig. 4I to L; Fig. S1L**). Collectively, these data showed that *Trp53*- and *Dnmt3a*-CH are associated with faster tissue repair after injury.

Distinct Prognosis of Acute CVD Patients with Clonal Hematopoiesis

To investigate the role of CH in acute CVDs among human cohorts, we analyzed whole-exome sequencing data from 52,338 and 73,628 acute CVD patients in the UK Biobank (UKB) and the All of Us research program (AoU). These two cohorts had median ages of 61 years (UKB) and 63 years (AoU) (**Fig. S2A**), with 1.4% of UKB patients (n = 734) and 3.5% AoU patients (n = 2,577) identified as CH carriers, defined by a variant allele frequency (VAF) of at least 0.02. As observed in previous studies, the prevalence of CH increased with age (**Fig. S2A and B**)[1,5]. We identified 70 distinct somatic mutations with a VAF of at least 0.02, displaying patterns in line with previous reports (**Fig. S2D to J**)[1,2,9,10,23]. The most frequent mutations occurred in *TET2, ASXL1,* and *DNMT3A* among the total acute CVD cohort or stratified by specific subtypes (**Fig. S2K**). Females and males were similarly affected overall; however, there were significant gene-level differences between sexes observed in *ASXL1*, *STAG2*, and *SRSF2* (**Fig. S1L**), reflecting the potential sex-specific differences in prevalence of these gene-level frequencies. We next performed a phenome-wide association study (PheWAS) of incident acute CVD or comorbidities in the UKB, considering CH at baseline as the exposure. This identified strong associations with *TET2, JAK2,* and *ASXL1*, but not *DNMT3A* or *TP53*, with acute CVDs (**Fig. S3A to D**). This observation suggests that different CH mutations may play distinct roles in the progression of acute CVDs. To explore this further, we assessed the relationship between specific CH mutations and rehospitalization rates and overall survival due to acute CVDs. We found no significant association between CH mutations and rehospitalization events (**Fig. S3E**). *ETV6*, *JAK2*, and *TET2* are associated with significantly worse survival, while no significant association with *DNMT3A* or *TP53* was observed (**Fig. S3F and G**). No significant difference in age was observed between individuals with *DNMT3A/TP53* or *TET2* mutations and non-CH carriers (**Fig. S3H**).

scRNA-Seq Reveals Increased T Cell Neutrophil Expansion

To understand how CH drives tissue repair, we performed single-cell RNA sequencing (scRNA-seq) of hematopoietic (CD45.2$^+$) and non-hematopoietic (CD45$^-$) cells from muscle tissue seven days post-HLI. Unbiased clustering revealed 11 distinct cell populations, including macrophages (*Adgre1*$^+$), fibroblasts (*Pdgfa*$^+$), B cells (*Cd19*$^+$), erythrocytes, neutrophils (*Ly6g*$^+$), T cells (*Cd3e*$^+$), NK cells (*Ncr1*$^+$), mast cells (*Cd200r3*$^+$), myoblasts (*Pax7*$^+$), myocytes (*Myh4*$^+$), endothelial cells (*Pecam1*$^+$), and neural cells (**Fig. 5A**), expressing canonical cell markers as well as gene signatures of unique cellular processes, respectively (**Fig. S4A and B**). In total, we analyzed a total of 21,853 (>6,000 per condition) cells from CH and Ctrl mice (n=6).

We first analyzed tissue cells undergoing regeneration, such as endothelial cells and muscle cells. Consistent with our prior data of faster vascular and muscle regeneration (**Fig. 3 and 4**), we found CH mice-derived endothelial cells and muscular cells show reduced tissue repair and myoblast gene signature, respectively, as well as a more terminal state in pseudotime trajectory analysis (**Fig. S4C to J**).

We then analyzed the hematopoietic composition of the single cells and found that CH mice exhibited higher fractions of T cells and neutrophils compared with control mice (**Fig. S5A**). We then performed flow cytometry and found higher absolute numbers of neutrophils in the peripheral blood (PB) and injury site of CH mice (**Fig. S5C and D**). T cells show comparable levels in the PB but increased levels in the injury site (**Fig. S5E and F**). Neutrophils and T cells were reported to promote tissue repair through the production of growth factors and recruiting macrophages to the injury site[24-27]. However, we found no significant differences in these factors

between individual mutant vs. WT cells (**Fig. S5G and H**). We further performed intra-cardiac transplantation of mutant and WT neutrophils or T cells and found no improvement in cardiac function (**Fig. S5I and J**), indicating an alternative cell type that drives the accelerated tissue repair in CH mice.

CH Mice-derived Fibroblasts Are Skewed Toward a Pro-Angiogenic State

To identify the major effectors of the enhanced tissue repair in CH mice, we compared cell-cell crosstalk, including hematopoietic cells and tissue cells, using CellChat[28]. We found fibroblasts and macrophages displayed the strongest communication strength (**Fig. 5B**). We first analyzed the differentially expressed signals between CH and Ctrl mice-derived fibroblasts and found upregulation of pro-regenerative signals, including VEGF, EGF, and IGF, in both CH mice-derived fibroblasts (**Fig. S6A and B**).

To further explore the role of fibroblasts in tissue repair, we conducted higher-resolution analysis, identifying three fibroblast clusters (**Fig. S6C**). Interestingly, clusters 1 and 2 were predominantly Ctrl mice-derived, while cluster 0 was enriched with both *Trp53* and *Dnmt3a* CH mice-derived fibroblasts, suggesting distinct functional states between the groups and that *Trp53* and *Dnmt3a* CH mice-derived fibroblasts share similar function, which is confirmed by principal component analysis (PCA) (**Fig. S6D**). GSEA revealed that CH mice-derived fibroblasts had downregulated gene signatures associated with fibroblast activation (**Fig. S6E and F**). Indeed, differential gene expression analysis showed that CH mice-derived fibroblasts show reduced expression of pro-fibrotic genes, such as *Col1a1*, *Col1a2*, *Col3a1*, etc. (**Fig. S6G**). This indicates that fibroblasts from CH and Ctrl mice adopt distinct functional roles[29-31], with Ctrl mice-derived fibroblasts favoring fibrosis and CH mice-derived fibroblasts promoting angiogenesis (**Fig. S6H**).

To validate our finding, we isolated fibroblasts from the left ventricle of mutant mice 7 days post-infarct[32] and quantified VEGF levels in fibroblast culture medium. We found a higher level of VEGF production by fibroblasts isolated from mutant mice (**Fig. S6I**). To functionally assess the proangiogenic ability of mutant mice derived fibroblasts, we assessed the effect of fibroblast conditioned media (CM) on promoting human umbilical vein endothelial cells (HUVEC) proliferation measured by HUVECs assembly into interconnected tubelike structures on a growth factor reduced matrix (vascular assembly), and found mutant mice derived fibroblasts CM increased vascular assembly compared with WT mice derived fibroblasts CM (**Fig. S6J**). Then, we intracardially injected mutant or WT mice-derived fibroblasts into WT CD45.1 mice immediately after LAD ligation to assess the in vivo function of CH-mice-derived fibroblasts. However, we found no functional improvement of LVEF in mice transplanted with mutant mice-derived fibroblasts (**Fig. S6K**).

Mutant Macrophages Exhibit Enhanced Tissue Repair Profile

Another type of cell that displayed strong communication strength is the macrophage (**Fig. 5B**), which is known to be central for tissue repair following injury[33]. We then assessed the transcriptome of mutant macrophages and found both *Trp53* and *Dnmt3a* mutant macrophages exhibited enhanced wound healing gene signatures (**Fig. 5C**). Again, similar to fibroblasts, higher-resolution analysis of macrophage found both *Trp53* and *Dnmt3a* mutant macrophages are enriched in shared clusters and suggests similar functional profile and distinction from WT macrophages (**Fig. 5D and E**). We next examined the gene expression (**Fig. 5F**), the developmental relationship between these macrophage clusters using diffusion map analysis (**Fig. 5G**), and hierarchical clustering analysis (**Fig. 5H and I**). Collectively, these approaches classified the macrophages into two subpopulations: MerTK^{+}Trem2^{lo} and MerTK^{-}Trem2^{hi}. The MerTK^{+}Trem2^{lo} macrophages comprise the subpopulations Folr2^{+}Lyve1^{+}, Trem2^{lo}Gdf5^{+}, and Trem2^{lo}Gdf15^{+}. MerTK^{-}Trem2^{hi} macrophages comprise subpopulations cycling macrophages, Vegfa^{+}, and Trem2^{hi}Folr2^{+} (**Fig. 5I**).

CH mice-derived macrophages are significantly enriched in Folr2^{+}Lyve1^{+} and Vegfa^{+} populations, while Ctrl mice-derived macrophages are significantly enriched in cycling, Trem2^{hi}Folr2^{+}, Trem2^{lo}Gdf5^{+}, and Trem2^{lo}Gdf15^{+} macrophages (**Fig. 5J**). Given the higher proportion of cycling macrophages in Ctrl mice, we analyzed the cell cycle status of all macrophages and found Ctrl mice-derived macrophages show a significantly higher proportion of macrophages undergoing cell division (**Fig. 5K and L**). To understand whether CH mice-derived macrophages are already after or yet to reach active cell division, we analyzed the pseudotime status and found CH mice-derived macrophages were at a more advanced stage of differentiation (**Fig. 5M and N**). We further profiled the single cell transcriptome of CH vs Ctrl mice hind limb muscle extracts without injury and found a comparable cell transcriptomic profile of mutant vs. WT cells, marked by similar UMAP distribution (**Fig. S7A**), minimal DEGs (**Fig. S7B and C**), non-significant GSEA score (**Fig. S7D**), and

similar pseudotime differentiation score (**Fig. S7E**), indicating that external stressors are required to elicit faster expansion of mutant macrophages.

Trp53 and *Dnmt3a* Mutant Macrophages Accelerate Tissue Repair

To confirm whether mutant macrophages show faster expansion, we examined macrophage infiltration in MI, HLI, and CTX models. Consistently, CH mice displayed higher macrophage density and faster macrophage expansion at injury sites compared to Ctrl mice (**Fig. 6A to D; Fig. S8A and B**). Notably, in CH mice, mutant ($CD45.2^+$) macrophages also show faster expansion than WT ($CD45.1^+$) macrophages, marked by increased chimerism compared with pre-injury (~60% to ~70%). (**Fig. 6E to G**).

Macrophage expansion follows a dedicated trajectory known as the myeloid response[33], initiated by the activation of HSPCs in the bone marrow and subsequent differentiation and proliferation of multipotent progenitors (MPPs), common myeloid progenitors (CMPs), granulocyte-monocyte progenitors (GMPs), and monocytes. To dissect this trajectory, we assessed monocyte and HSPC compartment changes through the process of tissue repair. Consistent with macrophage expansion, CH mice exhibited increased monocytes in PB, with faster expansion and greater chimerism in PB-derived monocytes compared to Ctrl mice (**Fig. S8C to G**). In the BM, all groups exhibited increased Lin^- ($B220^-$ $CD19^-$ $CD3^-$ $CD8^-$ $CD11b^-$ $Gr\text{-}1^-$ $TER119^-$ $NK1.1^-$) cells after injury, but the rise in CH mice was greater and more sustained, peaking at day 14 post-HLI (**Fig. S8H and I**). Myeloid progenitors (MPs; Lin^- Kit^+ $Sca1^-$) and the LSK population (Lin^- Kit^+ $Sca1^+$) also showed higher and more persistent increases in CH mice (**Fig. S8J to L**). MPPs, short-term HSCs (ST-HSCs), and long-term HSCs (LT-HSCs) were increased in CH mice (**Fig. S8M to P**), while CMPs demonstrated a brief dip followed by a quick recovery in CH mice (**Fig. S8Q to S**). The data further support the elicited macrophage expansion by tissue injury, highlighted by the robust myeloid response in CH mice.

Next, to assess whether mutant macrophages show higher VEGF production, we isolated macrophages from the injury site after FAL and found higher production of VEGF by *Trp53/Dnmt3a* mutant macrophages in vitro, compared with WT macrophages (**Fig. 6H**). In the HUVEC vascular assembly assay, *Trp53/Dnmt3a* mutant macrophage CM significantly increased vascular assembly (156.3/136.2 vs. 98.1 branch points/field of view; $p = 6.2\times10^{-9}/1.7\times10^{-8}$; Fig. 6H) compared with WT macrophages.

To functionally validate the role of CH macrophages in tissue repair, we performed bone marrow-derived macrophage (BMDM) transplantation experiments. BMDMs were isolated from *Trp53* mutant, *Dnmt3a* mutant, or WT 45.2 mice. In addition, we have included *Tet2* knockout mice as a positive control, due to the well-established relationship between loss of *Tet2* function and adverse cardiovascular outcomes[17,34]. BMDMs had phenotypic markers ($Gr\text{-}1^-$, $CD3^-$, $CD19^-$, $F4/80^+$, $CD11b^{hi}$, $CD11c^+$, $CD14^+$, $CD16/32^+$, $CD64^+$, $CD68^+$, MHC class II^+) of macrophages (**Fig. S9A**). Colony-forming unit assay analysis indicated minimal CFU-GM colonies and no BFU-E or CFU-GEMM colonies (**Fig. S9B**). BMDMs were then injected into WT CD45.1 mice immediately after FAL, CTX injection, or LAD ligation (**Fig. S9C**). Consistent with our CH model, we observed faster tissue repair in mice transplanted with *Trp53* and *Dnmt3a* mutant macrophages (**Fig. 6J to P**), but decreased tissue repair in those transplanted with *Tet2* KO BMDMs (**Fig. S9D to J**), compared to those receiving WT macrophages.

Furthermore, to understand whether increased VEGF production in mutant macrophages is responsible for the accelerated tissue repair, we generated three different short hairpin RNA (shRNAs) targeting *Vegfa* to functionally study the role of VEGF in mutant macrophages-mediated tissue repair. All shRNAs efficiently decreased the expression of *Vegfa* (**Fig. S10A**). We selected the one with the strongest knockdown (KD) efficiency (sh-*Vegfa*-1) to carry on to the following experiments and found *Vegfa*-KD rescued the enhanced tissue repair phenotype in mutant BMDM-transplanted mice (**Fig. S10B to I**).

Trp53 and *Dnmt3a* Mutant Macrophages Accelerate Tissue Repair Through E2F Repression

To understand the signaling pathways that drive the increased VEGF production and superior tissue repair function of mutant macrophages, we compared the signaling pathways between mutant and WT macrophages and found reduced E2F signaling in both comparisons (**Fig. 7A**). To consolidate this finding, we then utilized pySCENIC to identify transcription factors (TFs) and their putative downstream target genes (i.e., regulons) in each hematopoietic cell types[35]. We identified a total of 175 TFs and found E2F1, E2F2, and E2F3 exhibited consistently reduced regulon activity in all mutant hematopoietic cells (**Fig. S11A to C**)[36].

To identify the predominant binding motifs associated with these changes, we performed motif enrichment prediction. This analysis uncovered 11 differentially bound motifs, including one shared by E2F1, E2F2, and E2F3. Notably, this motif is associated with *Vegfa*, along with other genes, such as *Zfp367*, *Slc6a*, etc. (**Fig. S11D**). These data strongly indicate that reduced E2F-associated *Vegfa* repression enhanced tissue repair in CH mice, consistent with prior reports[37].

To validate this, we performed CUT&RUN profiling for E2F motif accessibility. Compared to controls, both *Trp53*- and *Dnmt3a*-mutant macrophages displayed widespread loss of E2F motif accessibility (**Fig. 7B**), including the *Vegfa* locus (**Fig. 7C**), consistent with E2F activity repression. We next examined the repressive histone mark H3K27me3 using CUT&Tag. CH macrophages exhibited broad loss of H3K27me3 compared to controls (**Fig. 7D**), including at the *Vegfa* locus (**Fig. 7E**), suggesting epigenetic de-repression enables sustained VEGFA expression by the E2F pathway suppression. To test whether E2F suppression is functionally required for the enhanced reparative phenotype, we ectopically expressed E2F in mutant macrophages and assessed tissue repair outcomes (**Fig. S11F**). We found E2F overexpression significantly reduced the reparative benefit by mutant BMDMs (**Fig. 7F to L**)

Together, these data demonstrate that *Trp53* and *Dnmt3a* mutations converge on a shared program of E2F repression in macrophages. This reprogramming facilitates VEGFA expression and promotes improved tissue repair across diverse injury contexts.

Discussion

CH has traditionally been associated with increased risks of various diseases, such as malignancies, cardiovascular disorders, and inflammatory diseases. However, emerging evidences suggest that CH may exhibit positive effects for certain diseases. For instance, Bouzid et al. reported a potential protective role of CH in Alzheimer's disease[23], Kang et al. found CH mutations could preserve CD8 T cell stemness during immunotherapy[38],and Bhattacharya et al, reported *DNMT3A*- and *TP53*-related CH were linked to reduced hazard ratios for both all-cause and ischemic stroke[39]. Here, our study presents evidence that *Trp53* and *Dnmt3a*-mutant CH promote tissue repair following injury, revealing a previously underappreciated regenerative potential of CH.

We analyzed the association between acute CVD prognosis and CH using a large human cohort. CH is well established as a risk factor for developing cardiovascular diseases[9,10]. It is also well accepted that CH drives worse clinical outcomes of a wide array of CVDs, such as atherosclerosis and heart failure[5,11]. However, two key distinctions set our analysis and study apart from prior studies: 1) Previous studies primarily examined CH as a risk factor for developing CVD[9] or assessed outcomes in individuals with chronic CVDs, such as arteriosclerosis and heart failures[12-14], or pooled both chronic and acute CVDs[12]. 2) In contrast, our study specifically focuses on the outcomes of acute CVD (see methods for a complete ICD9 and ICD10 codes used to identify acute CVDs in the UKB cohort) in CH patients, an aspect not previously addressed in the literature.

We found that *TET2* and *JAK2* mutations are associated with worse outcomes, while no significant association between *DNMT3A/TP53* mutations and outcomes was observed. This suggests that CH mutations may show context-dependent behaviors. One possibility is that *DNMT3A* and *TP53* mutant hematopoietic clones alter immune cell function in ways that reduce pro-thrombotic inflammation and plaque destabilization. In other words, unlike other CH drivers that aggressively promote thrombogenesis and plaque rupture, *DNMT3A* or *TP53* mutations might produce a more benign inflammatory profile[40]. In line with this, several genomics studies found no association between *DNMT3A* and incident CVDs or adverse CVD outcomes, including chronic CVDs[41,42]. Likewise, *TP53*-mutant clones, which typically expand under DNA damage stress and are often seen in cancer survivors[40], may not actively exacerbate atherogenesis or trigger clotting cascades as other mutations, such as *TET2*. Such divergence of CH's effects on post-ischemia regeneration is particularly evident in our models and prior reported mouse models[17] and highlights a novel insight of our study: not all clonal hematopoiesis mutations confer equal cardiovascular risk, and in some cases, they may even impart protective effects, underscoring the importance of focusing on the distinct roles of different CH mutations in different disease settings.

Two reports are directly contradictory to our study. Wang et al. reported that *DNMT3A* mutation is associated with worse outcomes of MI patients[14]. However, this study reports that *DNMT3A* mutations are significantly more common in individuals aged >80, whereas those without *DNMT3A* mutations are enriched in the <50 age group. Since age is a major prognostic factor in MI outcomes, it is difficult to conclude from this study that

DNMT3A mutations independently contribute to worse MI outcomes. Shumliakivska et al. reported adverse outcomes of *DNMT3A* CH in a mouse MI model[43]. However, this study presents key limitations that may undermine its conclusions: 1) The study used a human mutant *DNMT3A* knock-in mouse model, which retains wild-type mouse *Dnmt3a*, as previously demonstrated[44]. 2) This retention may limit donor cell expansion, preventing clonal outgrowth, consistent with the original report, which found no long-term clonal advantage of mutant h*DNMT3A* cells[44].

Beyond the positive role of CH in acute CVDs, our study underscores a critical aspect of CH biology – its response is likely context-dependent. Even the same CH mutations may exert distinct effects on diseases with subtle differences in pathology. While *Dnmt3a*/*Trp53*-mutant CH enhances recovery from acute ischemic injuries, such as those induced by LAD ligation or FAL, previous studies suggest that it worsens outcomes in chronic disease models, including angiotensin II-induced heart failure and arteriosclerosis[13,45]. This is supported by our observation of the pronounced monocytosis of *Dnmt3a* and *Trp53* clones that is not reported by these studies[13,45]. These divergent outcomes emphasize the importance of considering disease context when evaluating CH's role, as acute and chronic conditions likely engage distinct inflammatory and regenerative pathways. Understanding these context-dependent effects is crucial for developing targeted therapeutic strategies that account for the differential impact of CH mutations across various disease settings.

One potential explanation for the context-dependent roles of mutant hematopoietic cells is their responsiveness to external stimuli. Supporting this notion, several studies have reported stable hematopoietic stem and progenitor cell (LSK) counts in the BM and unchanged PB white blood cell (WBC) or myeloid cell frequencies despite clonal expansion, yet these cells exhibit distinctly altered differentiation trajectories following tissue injury or disease progression[3,8,13,17]. Acute and chronic cardiovascular diseases are known to induce unique cellular signaling environments, characterized by distinct inflammatory cytokine profiles[46], which likely differentially regulate mutant versus wild-type hematopoietic cells. An alternative hypothesis is that mutant hematopoietic cells possess a diminished capacity to resolve inflammation under persistent inflammatory conditions, particularly evident in chronic injury contexts. Indeed, mutations such as those in *TET2* markedly impair inflammation resolution, whereas TP53 and *DNMT3A* mutations may retain partial anti-inflammatory functionality compared to wild-type cells.

Our data also indicated increased mutant neutrophil and T cell expansion post-injury, which did not contribute significantly to improved tissue repair in our models. This is likely because neutrophils and T cells are transiently recruited to the injury site. The primary role of neutrophil is to facilitate the clearance of apoptotic tissue and the recruitment of macrophages, rather than directly promoting regeneration[47].Additionally, our single-cell RNA-seq data showed that *Dnmt3a* and *Trp53* mutations did not enhance the expression of pro-angiogenic genes in individual neutrophils, further supporting the conclusion that neutrophils are unlikely to be key mediators of the regenerative phenotype observed in CH-mutant models.

These insights suggest a promising avenue for macrophage-based therapy. Macrophages have long been recognized as key players in tissue repair, yet clinical trials using unengineered macrophage-based therapies have yielded limited success in conditions such as stroke (NCT01845350), anal fissures (NCT00507364), and peripheral artery disease (NCT00468000). Engineering macrophages to mimic the regenerative properties observed in *TP53*- and *DNMT3A*-mutant CH could enhance their reparative functions. Techniques, like CAR-M[48], have shown promise in cancer treatment and offer a viable platform for macrophage engineering to treat ischemic diseases. Importantly, as terminally differentiated cells, macrophages are not known to pose the risk of hematological malignancies, providing a favorable safety profile for future clinical use[49].

Our study presents several limitations. Our study only used female mice for in vivo experiments. This choice was made to minimize variability and potential confounding effects from sex-specific hormonal influences, particularly androgen signaling, which can impact immune cell development, inflammatory responses, and tissue repair. Using a single sex allowed for more controlled comparisons during the initial characterization of CH-driven regenerative phenotypes. However, the lack of male representation limits the generalizability of our findings. Further studies using age-matched male mice to evaluate whether the observed phenotypes are consistent across sexes are needed. These future experiments will help determine whether CH-driven tissue remodeling is modulated by sex and inform sex-specific therapeutic considerations.

Also, while our competitive transplantation model was initiated with a low percentage (10%) of mutant cells to mimic early CH, the observed clonal expansion to ~50% at the time of injury reflects the inherent growth advantage of *TP53* and *DNMT3A* mutant clones. This engraftment level may exceed the typical VAF observed

in human CH, and thus represents a later stage of clonal dominance. We acknowledge this limitation and emphasize that our model primarily captures the functional consequences of established clonal expansion rather than early, low-burden CH.

Methods

Mice

C57BL/6 (CD45.2), B6 CD45.1 mice were purchased from Charles River, Inc. The *Trp53*$^{R172H\text{-}wm}$ mice were gifts from Dr. Guillermina Lozano[18]. *The Dnmt3a*$^{fl\text{-}878H}$ mice were obtained from the Jackson Laboratory (stock #032289)[50]. The offspring were then crossed with Scl-CreER^{T} mice (stock #037466)[51], to obtain *Trp53*$^{R172H\text{-}wm}$; Scl-CreER^{T} or *Dnmt3a*$^{fl\text{-}878H}$; Scl-CreER^{T} mice. Mice were then induced with tamoxifen and then referred to as *Trp53*$^{R172H/+}$ or *Dnmt3a*$^{R878H/+}$ mice. Reagents will be made available through a material transfer agreement. Twelve-week-old female mice were used for in vivo experiments unless otherwise noted. Female mice were selected to minimize biological variability associated with sex-specific immune and regenerative responses, and to ensure consistency across cohorts for initial phenotypic characterization of CH-driven tissue repair. This approach also helps reduce potential confounding effects from androgen signaling known to modulate myeloid cell function and wound healing. Mice were maintained on a 12-h light/dark schedule in a specific pathogen-free animal facility and given food and water ad libitum. The number of mice included in each study is indicated in the figures or the associated legends. The Institutional Animal Care and Use Committee of the University of Missouri approved all study procedures.

UK Biobank

The UKB protocols were approved by the National Research Ethics Service Committee. Analyses in the UKB were conducted under approved project 106460. Participants signed written informed consent, specifically applicable to health-related research. All ethical regulations were followed. The UKB is a prospective longitudinal study containing in-depth genetic and health information from 500,000 UK participants. For this study, we have selected 52,338 individuals with acute CVD (ICD9: 4119, 436, 410, 411, 415, 420, 421, 422, 410-414, 433, 434, 3623, 4330, 4331, 4332, 4333, 4338, 4339, 4349, 444, 453, 673, 4151, 4341, 4440, 4441, 4442, 4448, 4449, 4532, 4533, 4538, 4539, 4109, 452, 4340, 4529, 6713, 6714, 59382, 6715, and 4376, and ICD10: I01.0, I01.1, I01.2, I01.8, I01.9, I21.0, I21.1, I21.2, I21.3, I21.4, I24.9, I30, I33, I30.9, I33.0, I33.9, I62.0, I63, I63.0, I63.3, I63.6, I63.8, I63.9, M62.2, M62.20, M62.21, M62.22, M62.23, M62.24, M62.25, M62.26, M62.27, M62.28, M62.29, K76.3, N28.0, D73.5, I24.0, I51.3, I74, I74.0, I74.1, I74.2, I74.3, I74.4, I74.5, I74.8, I74.9, I81, I82, I82.2, I82.3, I82.8, I82.9, K64, K64.5, O22.3, and O22.5) who had WES data available. Protocols for data collection and quality control have been described previously[52].

All of Us

AoU is an ongoing US-based observational cohort study[53]. AoU whole genome sequencing (WGS) data with median sequencing depth of 40x was available for 414,000 participants who were enrolled since 2017. These participants have linked health outcome data from participant survey questionnaires and electronic health records harmonized to the Observational Medical Outcomes Partnership (OMOP) Common Data Model (CDM) at enrollment and follow-up time points. For this study, we have selected 73,628 individuals with acute CVD (ICD9: 4119, 436, 410, 411, 415, 420, 421, 422, 410-414, 433, 434, 3623, 4330, 4331, 4332, 4333, 4338, 4339, 4349, 444, 453, 673, 4151, 4341, 4440, 4441, 4442, 4448, 4449, 4532, 4533, 4538, 4539, 4109, 452, 4340, 4529, 6713, 6714, 59382, 6715, and 4376, and ICD10: I01.0, I01.1, I01.2, I01.8, I01.9, I21.0, I21.1, I21.2, I21.3, I21.4, I24.9, I30, I33, I30.9, I33.0, I33.9, I62.0, I63, I63.0, I63.3, I63.6, I63.8, I63.9, M62.2, M62.20, M62.21, M62.22, M62.23, M62.24, M62.25, M62.26, M62.27, M62.28, M62.29, K76.3, N28.0, D73.5, I24.0, I51.3, I74, I74.0, I74.1, I74.2, I74.3, I74.4, I74.5, I74.8, I74.9, I81, I82, I82.2, I82.3, I82.8, I82.9, K64, K64.5, O22.3, and O22.5) who had WES data available.

Variant calling and annotation

Variant calling on WES/WGS data from was performed using Mutect2, Genome Analysis Toolkit (GATK) v.4.1.8.1[54]. Mutect2 was run in 'tumor-only' mode with default parameters, across the exons of 73 genes previously associated with CH[23]. To filter out potential germline variants we used germline variants generated from the 1000 Genomes Project (1000GP)[55] and the Genome Aggregation Database (gnomAD)[56] as reference. All resources were obtained from the GATK best practices repository (gs://gatk-best-practices/somatic-hg38). Raw variants called by Mutect2 were filtered out with FilterMutectCalls using the estimated prior probability of a reading orientation artifact generated by LearnReadOrientationModel (GATK v.4.1.8.1). Putative variants were filtered based on the following criteria: those flagged as 'PASS' using FilterMutectCalls or identified as 'germline' if present with the 'PASS' flag in at least two other samples. Gene annotation was conducted using the Ensembl Variant Effect Predictor (VEP; v.102)[57]. Variants were retained if they met the following thresholds: a minimum of two alternate reads, evidence on both forward and reverse strands, a read depth of at least seven for single nucleotide variants (SNVs) or 10 for short indels and substitutions, and a minor allele frequency (MAF) below 0.001 based on 1000 Genomes Project phase 3 and gnomAD r2.1 databases. Finally, output from the Mutect/Mutect2 pipelines was annotated for known clonal hematopoiesis variants within 73 genes from a curated whitelist (Supplementary Table 1).

Competitive bone marrow transplantation

Lethally irradiated CD45.1 recipients were transplanted with suspensions of BM cells containing 10% CD45.2^{+} *Trp53*$^{R172H/+}$ or *Dnmt3a*$^{R878H/+}$ cells and 90% CD45.1^{+} *Trp53*$^{+/+}$; *Dnmt3a*$^{+/+}$ cells (*Trp53* or *Dnmt3a* CH mice), or 10 % CD45.2^{+} *Trp53*$^{+/+}$; *Dnmt3a*$^{+/+}$ cells and 90% CD45.1^{+} *Trp53*$^{+/+}$; *Dnmt3a*$^{+/+}$ cells (Ctrl mice). BM cells were isolated from femurs and tibias of donor mice after euthanasia. Donor CD45.2^{+} cells were obtained from *Trp53*$^{R172H/+}$ or *Dnmt3a*$^{R878H/+,}$ or wild-type littermates. Donor CD45.1^{+} cells were obtained from B6 CD45.1 mice. Recipient B6 CD45.1 mice were irradiated in a pie cage to limit mobility and ensure equal dose of irradiation, and were exposed to two radiation doses of 550 rad three hours apart using an X-RAD 320 Biological Irradiator. After the second irradiation, each recipient mouse was injected with 10^{7} BM cells i.v.. Sterilized caging, food and water were provided during the first 14 days post-transplant and water was supplemented. Mice that did not recover full pre-irradiation body weight 28 days after transplant were excluded from further analysis. Thirteen weeks after BM transplantation, mice were subject to myocardial infarction, hind limb ischemia, or muscle injury. All injury model experiments included $\geqslant$5 mice per group, and key findings were independently replicated in at least two cohorts of transplanted mice. Mice with CD45.2^{+} engraftment falling outside of 50%-60% were excluded to ensure consistency across cohorts.

Myocardial infarction

Left anterior descending coronary artery (LAD) ligation was used to induced myocardial infarction as previously described[58]. Mice were anesthetized with 2% isoflurane inhalation. A small skin cut (1.2 cm) was made over the left chest, and a purse suture was made without tightening. After dissection and retraction of the pectoral major and minor muscle, the fourth intercostal space was exposed. A small hole was made at the fourth intercostal space with a mosquito clamp to open the pleural membrane and pericardium. With the clamp slightly open, the heart was smoothly and gently "popped out" through the hole. The LAD was located, sutured, and ligated at a site ≈3 mm from its origin using a 6-0 silk suture. Visualization of pale anterior wall of the LV was used to confirm successful ligation. After ligation, the heart was immediately placed back into the intrathoracic space followed by manual evacuation of air and closure of muscle and the skin, by tightening the previously placed purse-string suture. The mouse was then allowed to breath room air and monitored during the recovery period, which was generally complete within 3 to 5 minutes. No artificial respiratory aid was

required during the recovery time. The sham group underwent the same surgical procedure except that the LAD was not occluded. Hearts were collected before and at day 7, 14, 21, 28 after injury.

Hind limb ischemia

Femoral artery ligation was performed to induce hind limb ischemia in the mice as described[19]. Mice were anesthetized with isofluorane, and the animal's body temperature was maintained at 37±0.5°C. The left femoral artery was exposed through a 3-mm incision with minimal retraction and tissue disturbance. A 6.0-ligature was placed distal to the origin of the lateral caudal femoral and superficial epigastric arteries (the latter was also ligated) and proximal to the genu artery. The femoral artery was transected and separated by 1 to 2 mm between the sutures. The incision was cleaned and treated with saline before being closed. Laser Doppler perfusion imaging (LDPI, Moor Instruments) was used to confirm successful ligation. Hind limbs were collected before and at day 3, 7, 14, 21 after injury.

CTX muscle injury

Mice were anaesthetized with isoflurane and 50 μl of 10 μM CTX was injected in the tibialis anterior muscle[20]. Muscles were collected for analysis before and at day 1, 2, 3, 7, 14 after injury.

Echocardiography

For the evaluation of cardiac function, mice were anesthetized with 1% isoflurane, and analyzed with a Vevo 3100 High Resolution Imaging System (Visual Sonics Inc) equipped with a 30-MHz probe (MS550D) (VisualSonics). Echocardiographic parameters were measured under the long-axis M-mode when the heart rate was about 450 bpm. Left ventricular ejection fraction (LVEF) was calculated as previously described (dividing the stroke volume by the end-diastolic volume)[59].

Histology and quantification of area of interest

Mouse heart or muscle tissues were fixed in 4% PFA and sectioned. Samples were dehydrated, paraffin-embedded embedded and sectioned into 5 μm thick slices on a sliding microtome (Leica). For the heart, paraffin sections were cut through the entire ventricle from apex to base into serial sections at 0.4 mm intervals. For the muscle, sections were made transversely. Haematoxylin and eosin (H&E) staining and Masson's trichrome staining were performed according to standard procedures and used for the detection of fibrosis, necrosis, and muscle regeneration. Fibrosis size was quantified from at least 3 sections of the heart from ligature to apex and the average scar size for each heart was plotted. Necrotic muscle area was detected by H&E staining as the area that includes necrotic myocytes, inflammatory cells and interstitial cells. Images were captured with a Keyence BZ-X800 microscope with a 20× objective (resulting in approximately 200× magnification) and processed with ImageJ software (NIH).

Immunofluorescence

Mice hearts and muscles were fixed in 4% PFA for immunofluorescence (IF) analysis. Sections of 10 μm were obtained with a cryostat (Leica) and processed, and incubated with primary antibodies diluted in PBS, supplemented with 1% BSA and 1% Triton X-100 overnight at 4°C. After three 10-min washes with PBS, samples were stained for 1 h at room temperature with fluorescent secondary antibodies followed by 5 min of

DAPI staining (1μg/mL) for nucleus visualization. Slides were mounted with Immu-mount (Thermo Scientific) and viewed under a fluorescence microscope (Keyence BZ-8000) with a 20× objective, resulting in approximately 200× magnification. In all cell counting experiments, fields of view were randomized to reduce counting bias and 300 cells were considered per mouse. Primary antibodies used include: anti-Ki67 (1:200, ab15580, Abcam), anti-Aurkb (1:100, 611083, BD Transduction Laboratories), anti-cTnT (1:200, ab33589, Abcam), anti-CD31 (1:200, 102402, Biolegend), anti-SMA (1:200, MAB1420, R&D system), anti-caspase3 (1:200, #9662, Cell Signaling Technology), anti-eMyHC (1:20, DSHB), anti-Laminin (1:200, ab11575, Abcam), anti-Pax7 (1:20, DSHB), anti-pH3 (1:200, #9701, Cell Signaling Technology), anti-F4/80 (1:200, 123102, Biolegend).

Quantitative RT-PCR

RT-PCR was performed on 5 ng total RNA with gene-specific primers (as shown below) and a QIAGEN One Step RT-PCR kit (210210; Qiagen) according to the manufacturer's protocol. β-actin was used as the reference gene to normalize the relative expression for quantitative RT-PCR analysis. RT-qPCR primers used in this study were as follows: Pax7: forward (5'- TCTCCAAGATTCTGTGCCGAT -3') and reverse (5'-CGGGGTTCTCTCTCTTATACTCC-3'), Myog: forward (5'-GAGACATCCCCCTATTTCTACCA-3') and reverse (5'-GCTCAGTCCGCTCATAGCC-3'), *Vegfa*: forward (5'-CTGCCGTCCGATTGAGACC-3') and reverse (5'-CCCCTCCTTGTACCACTGTC-3'), E2f1: forward (5'-CTCGACTCCTCGCAGATCG-3') and reverse (5'-GATCCAGCCTCCGTTTCACC-3').

Virus infection and transfection

pLentiLoxp3.7 (addgene #11795) was used to construct *Vegfa* shRNA expressing lentiviral vectors. The target sequences for sh-*Vegfa*-1, sh-*Vegfa* -2, and sh-*Vegfa* -3 were 5'-GTTAATCGGTCTTTCCGGTGAC-3', 5'-GCAAGATCCGCAGACGTGTAAA-3', and 5'-GCAAGATCCGCAGACGTGTAAA-3', respectively. For the generation of E2F-1-overexpressing cells, BMDMs were transfected by electroporation with an expression vector (pLVX-CMV-IRES-EGFP-Puro) containing a wild-type E2F-1 cDNA insert. For virus packaging, virus constructs were mixed with pSPAX2 and pMD2.G (4:3:1), followed by transfection into 293T cells using PolyJet (SignaGen Laboratories). Virus-containing supernatant was collected 48-72 h post-transfection and used for infection as described previously[59]. For infection, BMDMs were suspended in virus supernatant supplemented with 4 μg/ml polybrene at 10^5/ml and placed in six-well plates for spin infection (2000 rpm, 90 min at 32 °C).

Laser Doppler perfusion imaging

Local blood perfusion in hind limbs was determined using laser Doppler perfusion imaging (LDPI, Moor Instruments) pre-operatively, 30 minutes post-operatively and at day 3, 7, 14, 21, and 28 post-operatively. Before imaging, excess hair was shaved from the limbs of mice, and the animals were placed on a heating pad set to 37 °C to reduce temperature variance. Blood flow in both ligated (left) and unligated (right) limb were monitored. Blood flow recovery was measured using the ratio of left ischemic limb blood flow/right normal limb blood flow.

Flowcytometry

Flow cytometry analysis of mouse PB, BM, and digested muscle, was carried out using BD Accuri C6 or Cytek Aurora. Cells were labelled with the following antibodies from Biolegend unless specifically indicated: Anti-CD3e-PE/Cyanine5 (mouse, #100310, 1:200 dilution), Anti-Ly-6G/Ly-6C (Gr-1)-PE/Cyanine5 (mouse, #108410, 1:200 dilution), Anti-CD11b-PE/Cyanine5 (mouse, #101210, 1:200 dilution), Anti-B220-PE/Cyanine5 (mouse, #103210, 1:200 dilution), Anti-CD117 (c-Kit)-APC (mouse, #105812, 1:200 dilution), Anti-Sca-1-PE-

Cyanine7 (mouse, #108114, 1:200 dilution), Anti-Ki67-FITC (mouse, #652410, 1:200 dilution), Anti-CD127(IL-7Rα)-PE/Cyanine5 (mouse, #135016, 1:200 dilution), Anti-CD16/32-PE (mouse, #101308, 1:200 dilution), Anti-CD45.1-PerCP/Cyanine5.5 (mouse, #110728, 1:200), Anti-CD45-APC (mouse, #103112, 1:200 dilution), Anti-CD45.1-PerCP/Cyanine5.5 (mouse, #110728, 1:200).

Muscle digestion

Tibialis anterior or gracilis muscles were dissected, minced, and digested using collagenase II (200x, HY-E70005B, MCE), Dispase II, (10x, MCE HY-131577), and 20 μg/mL DNase I (Roche, 10104159001) in DMEM for 1.5 h at 37 °C with gentle shaking. The digested tissue was filtered using a 40-μm-pore-sized mesh and cells were centrifuged 5 min at 500*g*. Cells were resuspended in PBS containing 2% FBS for flow cytometry staining or beads-based cell isolation for scRNAseq library preparation.

scRNAseq library preparation

CD45.2$^+$ cells were first enriched from digested muscles from CH or Ctrl mice with MoJoSort mouse CD45 isolation kit (480028, Biolegend). The ScaleBio Single Cell RNA Sequencing Kit v1.1 was used according to the manufacturer's instructions for scRNAseq library preparation[60]. Cells were fixed and loaded into the 96-well Indexed RT Oligo Plate according to the manufacturer's instructions[60]. For each mouse, 3,200 CD45$^-$ and 6,800 CD45.2$^+$ cells were used. Plate to add the RT barcode and UMI onto each transcript during reverse transcription. Each sample was loaded to a distinct set of wells to enable all samples to be processed on the same plate in a single batch. The cells from each well were then collected and pooled using the supplied collection funnel, mixed, and distributed across the 384-well Indexed Ligation Oligo Plate where the Ligation Barcode was added to each UMI-RT barcoded transcript. Then, the cells were once again collected and pooled using another collection funnel and counted with a hemocytometer with Trypan Blue. A total of 10,000 cells were distributed per well of the 96-well Final Distribution Plate. In each well, second strand synthesis was performed followed by a cleanup step. The PCR products were then tagmented followed by an indexing PCR step to add a third barcode to each well. 5ul from each of the 96 libraries were pooled and cleaned using 0.8X SPRIselect beads (B23317, Beckman Coulter). The average fragment size of the final library was quantified using a TapeStation 4200 (Agilent). The library concentration was quantified using the NEBNext Library Quant Kit for Illumina (E7630S, New England Biolands). The libraries were sequenced on a shared 25B flowcell on a NovaSeq X (Illumina) instrument to a target depth of 20,000 reads per cell.

scRNAseq analysis

Base calls were converted to fastq format and demultiplexed by Index1 barcode. Combinatorial barcode demultiplexing, barcode processing, adapter trimming, read mapping to the mm10 reference genome, single-cell counting, and generation of the feature-barcode matrices were done using ScaleBio Single-cell RNA Nextflow Workflow v1.6 (https://github.com/ScaleBio/ScaleRna). The count matrices were brought into Seurat for downstream analyses. For quality control, a UMI-gene cutoff of 500-4000 UMIs and 500 genes was used. The count matrices were log2-normalized, centered, and scaled using a scaling factor of 10,000. The top 2000 most variable genes were identified using dispersion and mean expression thresholds. PCA was then performed followed by dimensionality reduction by UMAP and unsupervised clustering using the Louvain algorithm using the FindClusters function of Seurat. Cluster marker genes were defined by grouping the clusters by genotype, setting logfc.threshold=0.5 and min.pct=0.2, and comparing the fold changes between pct.1 and pct.2 using FindMarkers. Cell type annotations were done referencing literature, cell identity

prediction using singleR[61], and single cell GSEA (scGSEA)[28]. Pseudobulk differential expression analysis between conditions within cell types was performed using DESeq2[62]. Pseudotime and trajectory analysis was done using Monocle3[63].

GSEA, leading-edge analysis, and scGSEA

The clusterProfiler in R version 4.4.0[64] was used to perform Gene set enrichment analysis (GSEA) and leading-edge analysis. Gene sets were obtained from the MSigDB (http://software.broadinstitute.org/gsea/msigdb/search.jsp). The differentially expressed genes obtained from FindMarkers function of Seurat with logfc.threshold=0.5 and min.pct=0.2 were used for analysis. Only GSEA results that were significant after correction were reported, with $q < 0.05$ being considered statistically significant. scGSEA scores of each cell were calculated using the RunMCA and RunCellHGT function in CellChat[28].

Cell-cell communication analysis

CellChat was used to infer cell-cell communications using the single-cell gene expression data and a database of prior knowledge of the interactions between signaling ligands, receptors, and their cofactors[28]. The CellChat database integrates the signaling molecule interaction information from KEGG and experimental studies. The curated interactions are categorized into 299 signaling pathways. CellChat predicts significant communication between cell groups (clusters) by identifying significantly over-expressed ligands and receptors between the cell groups. Communication probabilities were calculated using a mass action-based model based on the average expression values of a ligand and its cognate receptors from two cell groups. The signaling communication probabilities are modeled based on the proportions of cells in each cell group across all cells, as abundant cell groups are more likely to send stronger signals in comparison to rare groups. In the estimated cell-cell communication network with weights as probabilities, the major signaling roles are identified based on centrality metrics from graph theory. CellChat predicts the key sending and receiving signals between specific cell groups. The top 10% of significant cell-cell communications ($p < 0.05$) were selected across different pathways. The major sending and receiving signaling roles based on context-specific pathways across different cell groups were identified using a cut-off of 0.7 when visualizing the connection. The comparison between the overall information flow from the two study groups (CH versus Ctrl) was performed using the paired Wilcoxon test with the function rankNet from CellChat.

Primary neutrophil Isolation and transplantation

Bone marrow cells were harvested from femurs and tibias of euthanized mice. Bones were cleaned, sterilized in 70% ethanol, and flushed with RPMI 1640 supplemented with 10% FBS and 2 mM EDTA using a 25-gauge needle. Cells were centrifuged at 500 × g for 5 minutes at 4°C, then red blood cells were lysed using RBC lysis buffer (Abcam). After washing, cells were resuspended in PBS with 2% FBS and $CD11b^+Ly6G^+$ cells were sorted. For transplantation, immediately after LAD ligation, two doses of a total of 1×10^6 neutrophils were injected intramyocardially in the infarct border zone. The animals were placed on a heating pad and carefully observed until they achieved full locomotor behavior.

Primary T cell Isolation and transplantation

$CD3^+$ cells were enriched from RBC lysed spleen flush from euthanized mice with MoJoSort mouse CD3 isolation kit (Biolegend). After washing, cells were resuspended in PBS. For transplantation, immediately after

LAD ligation, two doses of a total of 1×10^6 T cells were injected intramyocardially in the infarct border zone. The animals were placed on a heating pad and carefully observed until they achieved full locomotor behavior.

Primary fibroblasts isolation and transplantation

Cardiac fibroblasts were isolated from infarct and peri-infarct regions of mouse hearts 7 days MI using an enzymatic digestion protocol[32]. Briefly, mice were euthanized and hearts perfused with cold PBS to remove blood. The left ventricle was dissected, minced into 1-2 mm pieces, and digested in a solution containing 2.5 mg/mL Collagenase II (Sigma) and 1 mg/mL Dispase II (Sigma) in HBSS supplemented with 20 mM HEPES and 1% penicillin/streptomycin. Tissue was incubated at 37°C for 30 minutes with gentle agitation. Digested tissue was filtered through a 70-µm, followed by a 40-µm cell strainer, centrifuged at 400g for 5 minutes, and red blood cells were lysed using RBC lysis buffer (Abcam). Cells were resuspended in DMEM with 10% FBS and plated for 1 hour. Non-adherent cells were washed away; adherent cells were maintained as fibroblast-enriched cultures. For flow cytometry assisted cell sorting, fibroblasts were defined as $CD45^-CD31^-PDGFR\alpha^+$ cells. For transplantation, immediately after LAD ligation, two doses of a total of 1×10^5 fibroblasts were injected intramyocardially in the infarct border zone. The animals were placed on a heating pad and carefully observed until they achieved full locomotor behavior.

SCENIC transcription factor regulon analysis

To infer transcription factor (TF) regulon activity, regulon analysis was performed using pySCENIC[35]. pySCENIC was run using the filtered, pre-processed raw counts as the input, and a list of workflow-supplied mouse TFs. Candidate regulons were pruned using the annotations of TF motifs ‘mm_motifs_to_TF_annotation.tbl’, and cisTarget was applied using the ‘mc_v10_clust’ databases of known mouse TF motifs annotated at: a) 500 bp upstream and 100 bp downstream of the transcription start site (TSS); and b) 10 kilobases centered around the TSS. No drop-out masking was applied. Enrichment of refined TF regulons was quantified using AUCell, with default parameters. Tests for differential regulon activity were performed using a linear mixed model, as described above.

Bone-marrow-derived macrophages (BMDMs)

Bone marrow cells were obtained from WT, *Trp53*$^{R172H/+}$ or *Dnmt3a*$^{R878H/+}$ mice by isolating and flushing tibias and femurs with DMEM (Life Technologies) containing 10% heat-inactivated FBS, 50 U/ml penicillin, and 50 µg/ml streptomycin. After red blood cells were removed with BD Pharm Lyse (BD Biosciences), mononuclear cells were isolated by centrifugation on Ficoll-Paque (GE Healthcare) at room temperature for 30 min, washed, re-suspended in DMEM containing 10% heat-inactivated FBS, 50 U/ml penicillin, and 50 µg/ml streptomycin, 10 ng/ml GM-CSF (R&D Systems) and 5 ng/ml M-CSF (R&D Systems), seeded into plastic dishes at a density of ~27×10^6 cells per 10 cm dish and cultured overnight at 37 °C in a humidified environment containing 5% CO_2. The next day, non- or weakly-adherent cells were recovered, transferred to a new dish and cultured under the conditions just described to permit differentiation and expansion of macrophages. Firmly adherent cells were discarded. After 2 days the culture medium was changed and after 5 days from seeding, adherent bone-marrow-derived macrophages were gently washed with PBS, harvested by brief exposure to trypsin-EDTA (Life Technologies), washed, and used for experiments. The cell purity was confirmed by analyzing $CD68^+$ and $F4/80^+$ cells with flow cytometry. For BMDM transplantation, immediately after operation (ligation or CTX injection), two doses of a total of 1×10^6 BMDMs were injected intramyocardially in the infarct border zone (MI), intramuscularly in the gracilis muscle (HLI), or intramuscularly in the tibialis

anterior muscle (CTX). The animals were placed on a heating pad and carefully observed until they achieved full locomotor behavior.

Colony-forming unit assay

BMDMs or bone marrow cells were seeded into M3434 medium (Stemcell Technologies). After 7 days in culture, colonies were examined morphologically under a microscope to identify and enumerate burst-forming erythroid progenitors (BFU-E), colony-forming myeloid progenitors (CFU-GM) and the multi-potential progenitors (CFU-GEMM).

In vitro vascular assembly assay

Human umbilical vein endothelial cells (HUVECs) were purchased from Lonza (C2519A; pooled donor) and were maintained in complete ECM medium (ScienCell). HUVECS (P5) were serum-starved with ECM containing 0.2% FBS overnight. Twenty-four well plates were coated with 150 µl of Matrigel (Corning) for 1 h at 37 °C. Following incubation, 3×10^4 HUVECS were seeded into each well with conditioned media collected from either mutant or WT fibroblasts or macrophages. After 16 h, images (×10) were taken using an EVOS M5000 (Thermo Fisher). Vascular assembly was assessed by counting the number of intersecting branches.

CUT&RUN

CUT&RUN was performed using CUT&RUN Assay Kit (Cell Signaling Technologies, #86652) according to manufacturer's instruction. Briefly, cells were harvested, washed, and bound to activated Concanavalin A-coated magnetic beads and permeabilized. The bead-cell complex was incubated overnight with the E2F1 (Santa Cruz, # sc-251) and rabbit IgG (Cell Signaling, #2729) antibody at 4°C. Cells were washed three times and resuspended in 100 µl pAG/MNase and incubated for 1 h at room temperature. DNA fragments were isolated by phenol/chloroform extraction followed by ethanol precipitation. CUT&RUN libraries were prepared using the DNA library prep kit for illumina systems (Cell Signaling Technologies, #56795) according to the manufacturer's instructions. Library quality was assessed using a Tapestation 4200 (Agilent). Sequencing was performed on an Illumina NovaSeq platform in 150 bp paired-end mode, with raw sequencing depths of 6 million reads.

CUT&Tag

The CUT&Tag experiments were performed following the CUT&Tag protocol[65]. For each targeted protein, 100,000 cells were used. The following primary antibodies were used at 1:50 dilution: H3K27me3 (Cell Signaling Technologies, #C36B11) and rabbit IgG (Cell Signaling, #2729). We used guinea pig anti-rabbit IgG (H+L) secondary antibody (NBP1- 72763) with 1:50 dilution. pA-Tn5 was bought from EpiCypher (15-1117). Final libraries were sequenced as 150-bp paired-end reads on a platform Novaseq X Plus, with raw sequencing depths of 6 million reads.

CUT&RUN and CUT&Tag data analysis

CUT&RUN sequencing reads were processed using ENCODE ChIP-seq pipeline. Specifically, reads were first trimmed by Trim_ Galore! using the "--paired" option and then aligned to GRCm39 with Bowtie2 (v.2.3.5.1). PCR duplicates were removed using the Picard MarkDuplicates tool with "VALIDATION_STRINGENCY=LENIENT" option. MACS2 (v.2.2.4) was used for peak calling for histone marks and TFs with "-p 1e-2 --nomodel --shift 0 --keep-dup all -B --SPMR" options. Peaks in the ENCODE hg38 blacklist regions (http://mitra.stanford.edu/kundaje/akundaje/release/blacklists/hg38-human/hg38.blacklist.bed.gz) were filtered out. Peaks with MACS2-reported q value < 10^{-5} were retained for downstream analyses. The output was visualized using chipseq and Gviz in R[66].

Statistical analysis

Data are shown as mean ± sd unless otherwise stated. Statistical significance of differences in experiments with two groups and only one variable was assessed by unpaired Student's t tests (with Welch correction for unequal variance when appropriate) or Mann-Whitney U Tests. Differences in experiments with more than one independent variable were evaluated by two-way analysis of variance (ANOVA) with post-hoc Sidak's or Tukey's multiple comparison tests. All statistical tests were performed using R.

References

1 Jaiswal, S. *et al.* Age-related clonal hematopoiesis associated with adverse outcomes. *N Engl J Med* **371**, 2488-2498, doi:10.1056/NEJMoa1408617 (2014).

2 Xie, M. *et al.* Age-related mutations associated with clonal hematopoietic expansion and malignancies. *Nat Med* **20**, 1472-1478, doi:10.1038/nm.3733 (2014).

3 Wang, H. *et al.* Clonal hematopoiesis driven by mutated DNMT3A promotes inflammatory bone loss. *Cell*, doi:10.1016/j.cell.2024.05.003 (2024).

4 Jakobsen, N. A. *et al.* Selective advantage of mutant stem cells in human clonal hematopoiesis is associated with attenuated response to inflammation and aging. *Cell Stem Cell* **31**, 1127-1144 e1117, doi:10.1016/j.stem.2024.05.010 (2024).

5 Calvillo-Arguelles, O. *et al.* Cardiovascular Disease Among Patients With AML and CHIP-Related Mutations. *JACC CardioOncol* **4**, 38-49, doi:10.1016/j.jaccao.2021.11.008 (2022).

6 Agrawal, M. *et al.* TET2-mutant clonal hematopoiesis and risk of gout. *Blood* **140**, 1094-1103, doi:10.1182/blood.2022015384 (2022).

7 Kim, M. J. *et al.* Clonal hematopoiesis as a novel risk factor for type 2 diabetes mellitus in patients with hypercholesterolemia. *Front Public Health* **11**, 1181879, doi:10.3389/fpubh.2023.1181879 (2023).

8 Kim, P. G. *et al.* Dnmt3a-mutated clonal hematopoiesis promotes osteoporosis. *J Exp Med* **218**, doi:10.1084/jem.20211872 (2021).

9 Jaiswal, S. *et al.* Clonal Hematopoiesis and Risk of Atherosclerotic Cardiovascular Disease. *N Engl J Med* **377**, 111-121, doi:10.1056/NEJMoa1701719 (2017).

10 Genovese, G. *et al.* Clonal hematopoiesis and blood-cancer risk inferred from blood DNA sequence. *N Engl J Med* **371**, 2477-2487, doi:10.1056/NEJMoa1409405 (2014).

11 Dorsheimer, L. *et al.* Association of Mutations Contributing to Clonal Hematopoiesis With Prognosis in Chronic Ischemic Heart Failure. *JAMA Cardiol* **4**, 25-33, doi:10.1001/jamacardio.2018.3965 (2019).

12 Gumuser, E. D. *et al.* Clonal Hematopoiesis of Indeterminate Potential Predicts Adverse Outcomes in Patients With Atherosclerotic Cardiovascular Disease. *J Am Coll Cardiol* **81**, 1996-2009, doi:10.1016/j.jacc.2023.03.401 (2023).

13 Zekavat, S. M. *et al.* TP53-mediated clonal hematopoiesis confers increased risk for incident atherosclerotic disease. *Nat Cardiovasc Res* **2**, 144-158, doi:10.1038/s44161-022-00206-6 (2023).

14 Wang, S. *et al.* Prevalence and prognostic significance of DNMT3A- and TET2- clonal haematopoiesis-driver mutations in patients presenting with ST-segment elevation myocardial infarction. *EBioMedicine* **78**, 103964, doi:10.1016/j.ebiom.2022.103964 (2022).

15 Raphael, C. E. *et al.* Causes of Death After Type 2 Myocardial Infarction and Myocardial Injury. *J Am Coll Cardiol* **78**, 415-416, doi:10.1016/j.jacc.2021.05.026 (2021).

16 Marston, N. A. *et al.* Clonal hematopoiesis, cardiovascular events and treatment benefit in 63,700 individuals from five TIMI randomized trials. *Nat Med* **30**, 2641-2647, doi:10.1038/s41591-024-03188-z (2024).

17 Sano, S. *et al.* Tet2-Mediated Clonal Hematopoiesis Accelerates Heart Failure Through a Mechanism Involving the IL-1beta/NLRP3 Inflammasome. *J Am Coll Cardiol* **71**, 875-886, doi:10.1016/j.jacc.2017.12.037 (2018).

18 Zhang, Y. *et al.* Somatic Trp53 mutations differentially drive breast cancer and evolution of metastases. *Nat Commun* **9**, 3953, doi:10.1038/s41467-018-06146-9 (2018).

19 Wang, C. *et al.* Repair of Limb Ischemia Is Dependent on Hematopoietic Stem Cell Specific-SHP-1 Regulation of TGF-beta1. *Arterioscler Thromb Vasc Biol* **43**, 92-108, doi:10.1161/ATVBAHA.122.318205 (2023).

20 Seo, B. R. *et al.* Skeletal muscle regeneration with robotic actuation-mediated clearance of neutrophils. *Sci Transl Med* **13**, eabe8868, doi:10.1126/scitranslmed.abe8868 (2021).
21 von Maltzahn, J., Jones, A. E., Parks, R. J. & Rudnicki, M. A. Pax7 is critical for the normal function of satellite cells in adult skeletal muscle. *Proc Natl Acad Sci U S A* **110**, 16474-16479, doi:10.1073/pnas.1307680110 (2013).
22 Zammit, P. S. Function of the myogenic regulatory factors Myf5, MyoD, Myogenin and MRF4 in skeletal muscle, satellite cells and regenerative myogenesis. *Semin Cell Dev Biol* **72**, 19-32, doi:10.1016/j.semcdb.2017.11.011 (2017).
23 Bouzid, H. *et al.* Clonal hematopoiesis is associated with protection from Alzheimer's disease. *Nat Med* **29**, 1662-1670, doi:10.1038/s41591-023-02397-2 (2023).
24 Bijnen, M. *et al.* Adipose tissue macrophages induce hepatic neutrophil recruitment and macrophage accumulation in mice. *Gut* **67**, 1317-1327, doi:10.1136/gutjnl-2016-313654 (2018).
25 Christoffersson, G. *et al.* VEGF-A recruits a proangiogenic MMP-9-delivering neutrophil subset that induces angiogenesis in transplanted hypoxic tissue. *Blood* **120**, 4653-4662, doi:10.1182/blood-2012-04-421040 (2012).
26 Nadkarni, S. *et al.* Neutrophils induce proangiogenic T cells with a regulatory phenotype in pregnancy. *Proc Natl Acad Sci U S A* **113**, E8415-E8424, doi:10.1073/pnas.1611944114 (2016).
27 Manetti, M. *et al.* Angiogenic T cell expansion correlates with severity of peripheral vascular damage in systemic sclerosis. *PLoS One* **12**, e0183102, doi:10.1371/journal.pone.0183102 (2017).
28 Jin, S. *et al.* Inference and analysis of cell-cell communication using CellChat. *Nat Commun* **12**, 1088, doi:10.1038/s41467-021-21246-9 (2021).
29 Kantari-Mimoun, C. *et al.* Resolution of liver fibrosis requires myeloid cell-driven sinusoidal angiogenesis. *Hepatology* **61**, 2042-2055, doi:10.1002/hep.27635 (2015).
30 Shaw, T. J. & Martin, P. Wound repair at a glance. *J Cell Sci* **122**, 3209-3213, doi:10.1242/jcs.031187 (2009).
31 Häkkinen, L., Larjava, H. & Koivisto, L. Granulation tissue formation and remodeling. *Endodontic Topics* **24**, 94-129, doi:https://doi.org/10.1111/etp.12008 (2011).
32 Almazloum, A. & Khalil, H. Isolation of Adult Mouse Cardiac Fibroblasts. *Curr Protoc* **3**, e840, doi:10.1002/cpz1.840 (2023).
33 Yap, J. *et al.* Macrophages in cardiac remodelling after myocardial infarction. *Nat Rev Cardiol* **20**, 373-385, doi:10.1038/s41569-022-00823-5 (2023).
34 Fuster, J. J. *et al.* Clonal hematopoiesis associated with TET2 deficiency accelerates atherosclerosis development in mice. *Science* **355**, 842-847, doi:10.1126/science.aag1381 (2017).
35 Bravo Gonzalez-Blas, C. *et al.* SCENIC+: single-cell multiomic inference of enhancers and gene regulatory networks. *Nat Methods* **20**, 1355-1367, doi:10.1038/s41592-023-01938-4 (2023).
36 Attwooll, C., Lazzerini Denchi, E. & Helin, K. The E2F family: specific functions and overlapping interests. *EMBO J* **23**, 4709-4716, doi:10.1038/sj.emboj.7600481 (2004).
37 Zhu, H., Wang, G. & Qian, J. Transcription factors as readers and effectors of DNA methylation. *Nat Rev Genet* **17**, 551-565, doi:10.1038/nrg.2016.83 (2016).
38 Kang, T. G. *et al.* Epigenetic regulators of clonal hematopoiesis control CD8 T cell stemness during immunotherapy. *Science* **386**, eadl4492, doi:10.1126/science.adl4492 (2024).
39 Bhattacharya, R. *et al.* Clonal Hematopoiesis Is Associated With Higher Risk of Stroke. *Stroke* **53**, 788-797, doi:10.1161/STROKEAHA.121.037388 (2022).
40 Yura, Y., Sano, S. & Walsh, K. Clonal Hematopoiesis: A New Step Linking Inflammation to Heart Failure. *JACC Basic Transl Sci* **5**, 196-207, doi:10.1016/j.jacbts.2019.08.006 (2020).
41 Yu, B. *et al.* Supplemental Association of Clonal Hematopoiesis With Incident Heart Failure. *J Am Coll Cardiol* **78**, 42-52, doi:10.1016/j.jacc.2021.04.085 (2021).
42 Schuermans, A. *et al.* Clonal haematopoiesis of indeterminate potential predicts incident cardiac arrhythmias. *Eur Heart J* **45**, 791-805, doi:10.1093/eurheartj/ehad670 (2024).

43 Shumliakivska, M. *et al.* DNMT3A clonal hematopoiesis-driver mutations induce cardiac fibrosis by paracrine activation of fibroblasts. *Nat Commun* **15**, 606, doi:10.1038/s41467-023-43003-w (2024).
44 Scheller, M. *et al.* Hotspot DNMT3A mutations in clonal hematopoiesis and acute myeloid leukemia sensitize cells to azacytidine via viral mimicry response. *Nat Cancer* **2**, 527-544, doi:10.1038/s43018-021-00213-9 (2021).
45 Sano, S. *et al.* CRISPR-Mediated Gene Editing to Assess the Roles of Tet2 and Dnmt3a in Clonal Hematopoiesis and Cardiovascular Disease. *Circ Res* **123**, 335-341, doi:10.1161/CIRCRESAHA.118.313225 (2018).
46 Feghali, C. A. & Wright, T. M. Cytokines in acute and chronic inflammation. *Front Biosci* **2**, d12-26, doi:10.2741/a171 (1997).
47 Wang, J. Neutrophils in tissue injury and repair. *Cell Tissue Res* **371**, 531-539, doi:10.1007/s00441-017-2785-7 (2018).
48 Niu, Z. *et al.* Chimeric antigen receptor-modified macrophages trigger systemic anti-tumour immunity. *J Pathol* **253**, 247-257, doi:10.1002/path.5585 (2021).
49 Arumugam, P. *et al.* Long-Term Safety and Efficacy of Gene-Pulmonary Macrophage Transplantation Therapy of PAP in Csf2ra(-/-) Mice. *Mol Ther* **27**, 1597-1611, doi:10.1016/j.ymthe.2019.06.010 (2019).
50 Loberg, M. A. *et al.* Sequentially inducible mouse models reveal that Npm1 mutation causes malignant transformation of Dnmt3a-mutant clonal hematopoiesis. *Leukemia* **33**, 1635-1649, doi:10.1038/s41375-018-0368-6 (2019).
51 Gothert, J. R. *et al.* In vivo fate-tracing studies using the Scl stem cell enhancer: embryonic hematopoietic stem cells significantly contribute to adult hematopoiesis. *Blood* **105**, 2724-2732, doi:10.1182/blood-2004-08-3037 (2005).
52 Sudlow, C. *et al.* UK biobank: an open access resource for identifying the causes of a wide range of complex diseases of middle and old age. *PLoS Med* **12**, e1001779, doi:10.1371/journal.pmed.1001779 (2015).
53 All of Us Research Program, I. *et al.* The "All of Us" Research Program. *N Engl J Med* **381**, 668-676, doi:10.1056/NEJMsr1809937 (2019).
54 Van Hout, C. V. *et al.* Exome sequencing and characterization of 49,960 individuals in the UK Biobank. *Nature* **586**, 749-756, doi:10.1038/s41586-020-2853-0 (2020).
55 Genomes Project, C. *et al.* A global reference for human genetic variation. *Nature* **526**, 68-74, doi:10.1038/nature15393 (2015).
56 Karczewski, K. J. *et al.* The mutational constraint spectrum quantified from variation in 141,456 humans. *Nature* **581**, 434-443, doi:10.1038/s41586-020-2308-7 (2020).
57 McLaren, W. *et al.* The Ensembl Variant Effect Predictor. *Genome Biol* **17**, 122, doi:10.1186/s13059-016-0974-4 (2016).
58 Gao, E. *et al.* A novel and efficient model of coronary artery ligation and myocardial infarction in the mouse. *Circ Res* **107**, 1445-1453, doi:10.1161/CIRCRESAHA.110.223925 (2010).
59 Pan, Y. *et al.* Inhibiting AGTR1 reduces AML burden and protects the heart from cardiotoxicity in mouse models. *Science Translational Medicine* **16**, eadl5931, doi:10.1126/scitranslmed.adl5931 (2024).
60 Mulqueen, R. M. *et al.* High-content single-cell combinatorial indexing. *Nat Biotechnol* **39**, 1574-1580, doi:10.1038/s41587-021-00962-z (2021).
61 Aran, D. *et al.* Reference-based analysis of lung single-cell sequencing reveals a transitional profibrotic macrophage. *Nat Immunol* **20**, 163-172, doi:10.1038/s41590-018-0276-y (2019).
62 Love, M. I., Huber, W. & Anders, S. Moderated estimation of fold change and dispersion for RNA-seq data with DESeq2. *Genome Biol* **15**, 550, doi:10.1186/s13059-014-0550-8 (2014).

63 Trapnell, C. *et al*. The dynamics and regulators of cell fate decisions are revealed by pseudotemporal ordering of single cells. *Nat Biotechnol* **32**, 381-386, doi:10.1038/nbt.2859 (2014).
64 Wu, T. *et al*. clusterProfiler 4.0: A universal enrichment tool for interpreting omics data. *Innovation (Camb)* **2**, 100141, doi:10.1016/j.xinn.2021.100141 (2021).
65 Kaya-Okur, H. S., Janssens, D. H., Henikoff, J. G., Ahmad, K. & Henikoff, S. Efficient low-cost chromatin profiling with CUT&Tag. *Nat Protoc* **15**, 3264-3283, doi:10.1038/s41596-020-0373-x (2020).
66 chipseq: chipseq: A package for analyzing chipseq data. R package version 1.50.0. (2023).

Author Contributions

Y.P. conceived the project, performed, and designed experiments, analyzed results, and produced the figures. X.M., W.Z., and C.W. performed and analyzed of results. Y.P. performed the bioinformatic and biostatistical analyses. X.M., W.Z., and C.W., conducted in vitro cell culture, infection and transfection RT-PCR, in vivo sample collection, and flowcytometry. Y.P., C.W., and X.M. performed histological experiments and surgical procedures. X.M., C.W., and W.Z. contributed to basic technical support such as cell sorter and flowcytometry. Y.P. prepared NGS library and deep sequencing. W.Z. and Q.Z. conducted echocardiogram. J.C. performed HUVEC assays. C.W performed laser doppler assay. All authors made comments and suggestions on data quality and helped edit the draft of the manuscript. X.K. provided funding. Y.P. wrote the original draft. All authors contributed to reviewing and editing. X.K. supervised the project.

Competing interests: The authors declare no competing interests.

Data and materials availability

All data associated with this study are present in the paper or supplementary materials. All sequence datasets generated in the current study have been deposited in NCBI SRA database with the bio project ID PRJNA1199521.

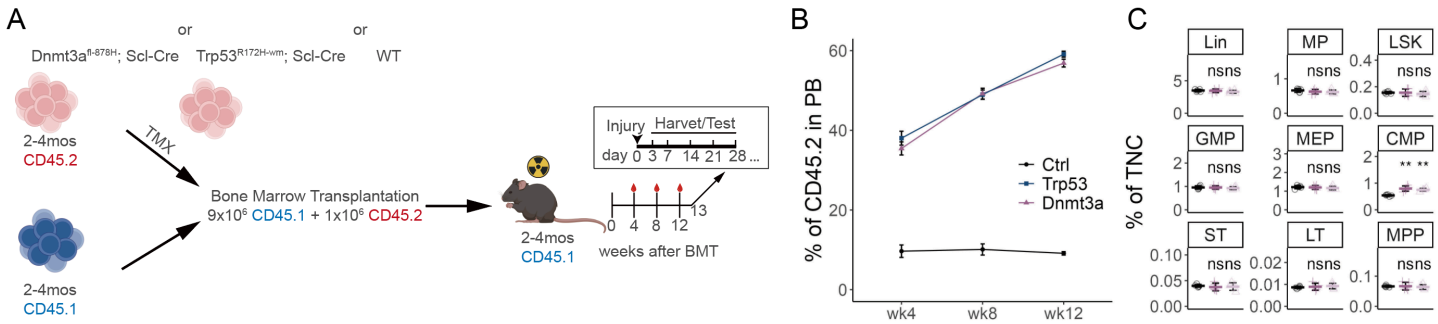

Figure 1. Clonal expansion driven by *Trp53* and *Dnmt3a* mutations

A, Schematic diagram for creating the CH and Ctrl mouse model and subsequent injury and data harvest.

B, Flow cytometry shows the fraction of CD45.2^{+} cells after bone marrow transplantation.

C, Quantification of HSPCs in flow cytometry in established CH mice at week 13. n = 5. Graphs are mean±sd. Student's t test.

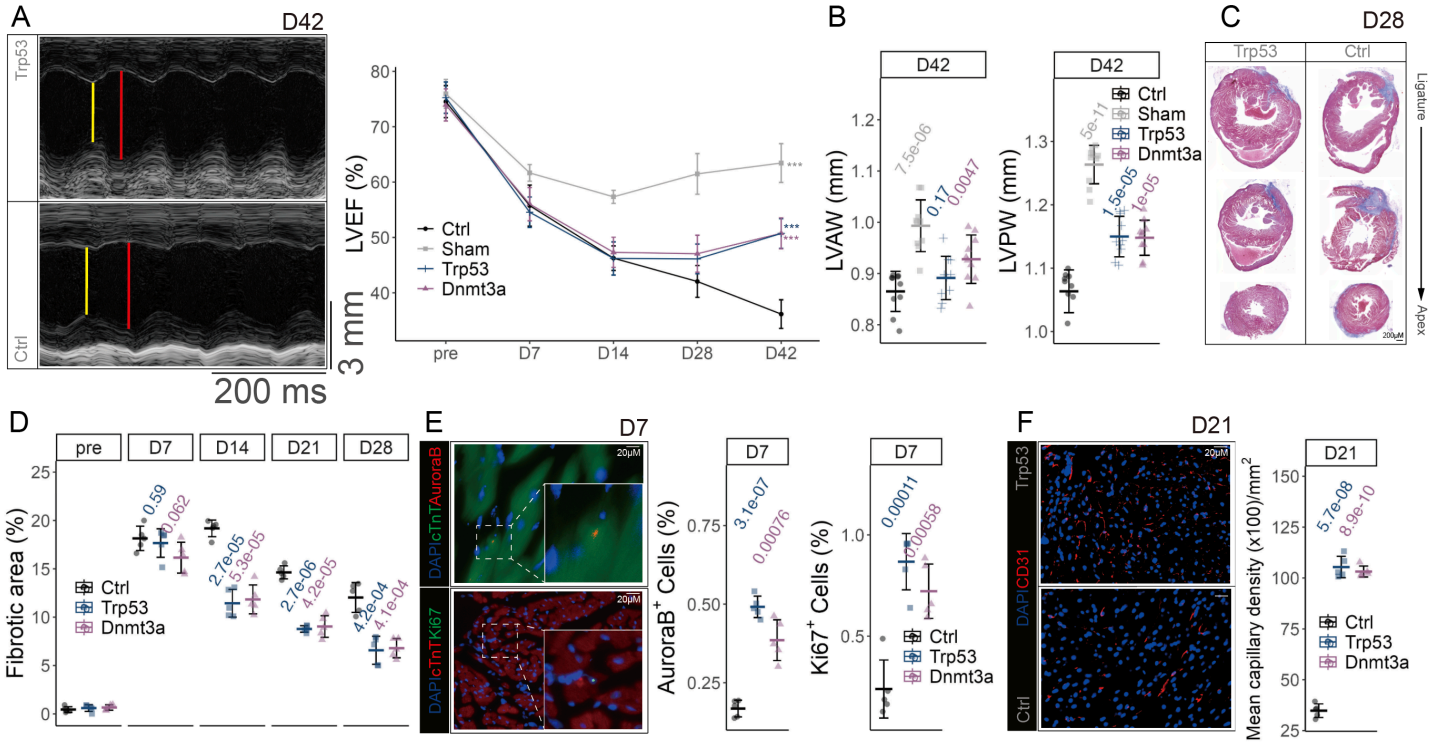

Figure 2. Clonal hematopoiesis enhances cardiac repair after myocardial infarction

A, Representative M-mode echocardiographic images of hearts and quantification of left ventricular ejection fraction (LVEF) of CH or Ctrl mice after left anterior descending artery (LAD) ligation (n=10). Yellow and red lines indicate left ventricular end-diastolic diameter and left ventricular end-systolic diameter, respectively. Scale bars, 200 ms, 3 mm. Two-way ANOVA with post-hoc Tukey's multiple comparison tests.

B, Quantification of left ventricular anterior wall (LVAW) and left ventricular posterior wall (LVPW) thickness in echocariograph after LAD ligation (n=10).

C and D, Representative images (trichrome) and quantification of fibrotic area from serial sections from ligature to apex after LAD ligation (n=5), Scale bar: 200 μM. pre, pre-ligation.

E, Representative image and quantification of cardiomyocyte cell-cycle re-entry in the peri-infarct region after LAD ligation by AuroraB (n = 2,321 cardiomyocytes from 5 mice) or Ki67 (n = 2,482 cardiomyocytes from 5 mice). Scale bar: 20 μM.

F, Representative image and quantification of myocardium vasculature in the peri-infarct region after LAD ligation by CD31 (n=5). Scale bar: 20 μM. Graphs are mean±sd.

Graphs are mean±sd. In all figures, n refers to the number of mice unless noted. P values are annotated. pre, pre-ligation. Data are compared using Student's t test unless noted.

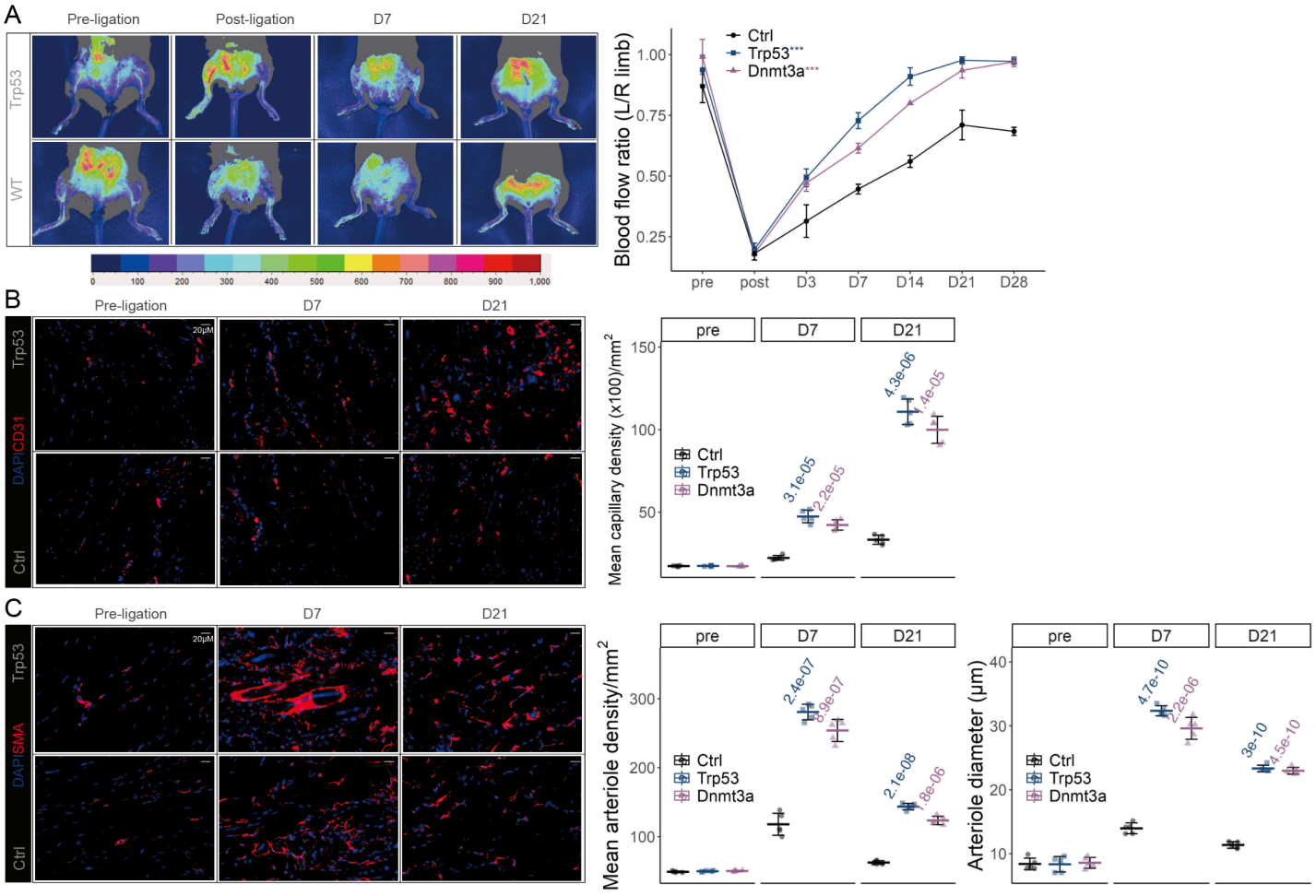

Figure 3. Clonal hematopoiesis promotes vascular regeneration after hind limb ischemia

A, Representative images of mouse hind limb blood flow measured with laser Doppler perfusion imaging before ligation, immediately after ligation, and day 7, 21 after ligation and continuous quantification of the blood flow ratio of left (ligated) versus right (un-ligated) limb (n=5). Two-way ANOVA with post-hoc Tukey's multiple comparison tests.

B, Representative images and quantification of CD31 staining to measure the capillary density on ischemic limb muscle (n=5), Scale bar: 20 μM. B, Representative images and quantification of CD31 staining to measure the capillary density on ischemic limb muscle (n=5), Scale bar: 20 μM.

C, Representative images and quantification of smooth muscle α-actin (SMA) staining to measure the arteriole density on ischemic limb muscle (n=5), Scale bar: 20 μM.

Graphs are mean±sd. In all figures, n refers to the number of mice unless noted. P values are annotated. pre, pre-ligation. post, immediately post-ligation. Data are compared using Student's t test unless noted.

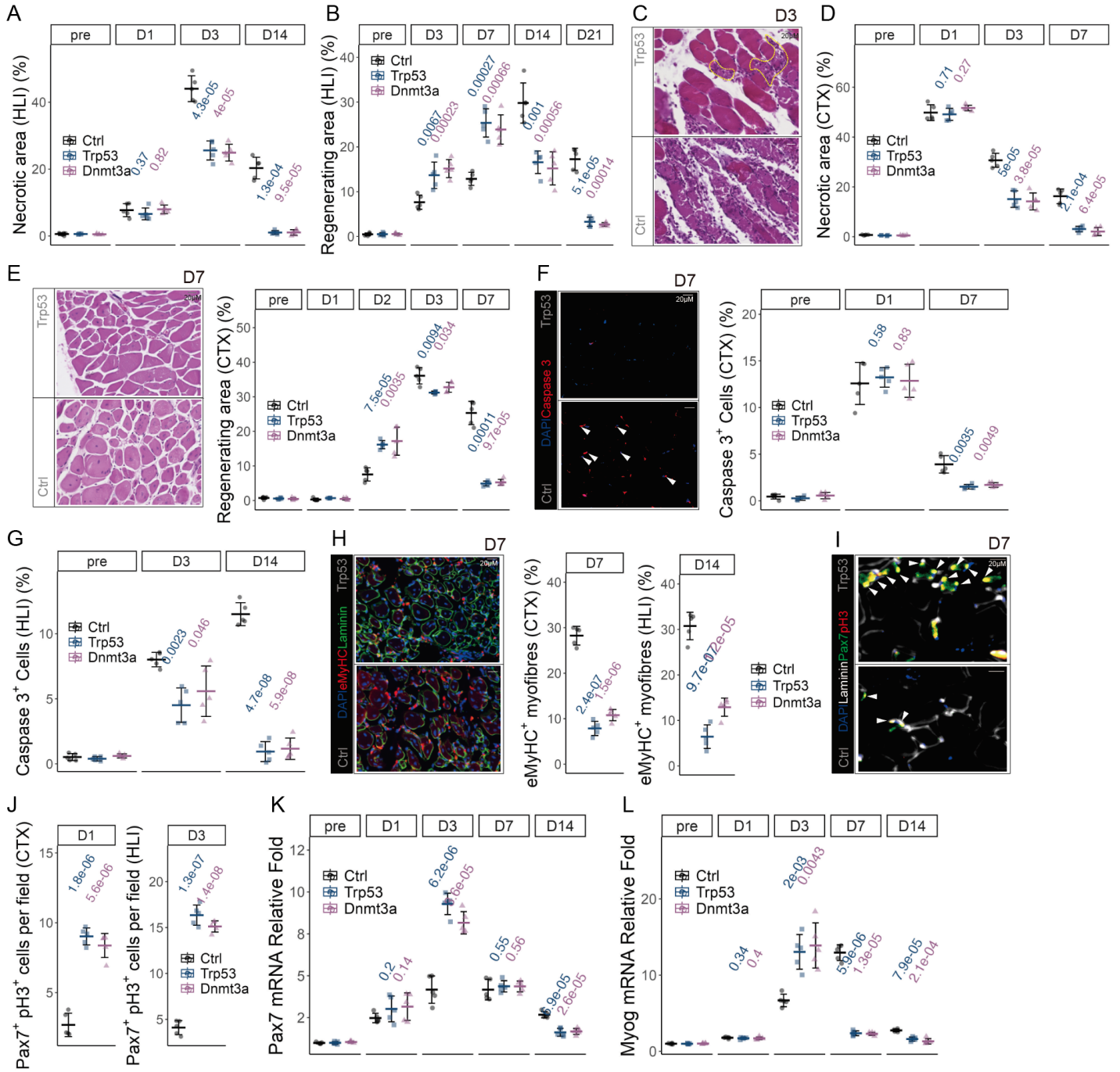

Figure 4. Clonal hematopoiesis accelerates muscle regeneration in ischemic and non-ischemic models

A and B, Quantification of muscle necrosis and regeneration at various time points in HLI model (n=5).

C and D, Representative images (H&E) and quantification of necrosis area in CTX model (n=5), Scale bar: 20 μM.

E, Representative images (H&E) and quantification of the regenerating area in CTX model (n=5), Scale bar: 20 μM.

F and G, Representative images and quantification of Caspase3 staining to measure muscle cell death in CTX and HLI models (n=5). Scale bar: 20 μM.

H, Representative images and quantification of eMyHC staining to measure the early and late regenerating muscle fibers in CTX and HLI models (n=5). Scale bar: 20 μM.

I and J, Representative images and quantification of Pax7 and pH3 staining to measure the muscle satellite cells in CTX and HLI models (n=5). Arrowheads, $Pax7^{+}pH3^{+}$ cells. Scale bar: 20 μM.

K and L, qPCR shows the expression of Pax7 and Myog in muscle extracts.

Graphs are mean±sd. In all figures, n refers to the number of mice unless noted. P values are annotated. All representative images are from the CTX model. Data are compared using Student’s t test unless noted.

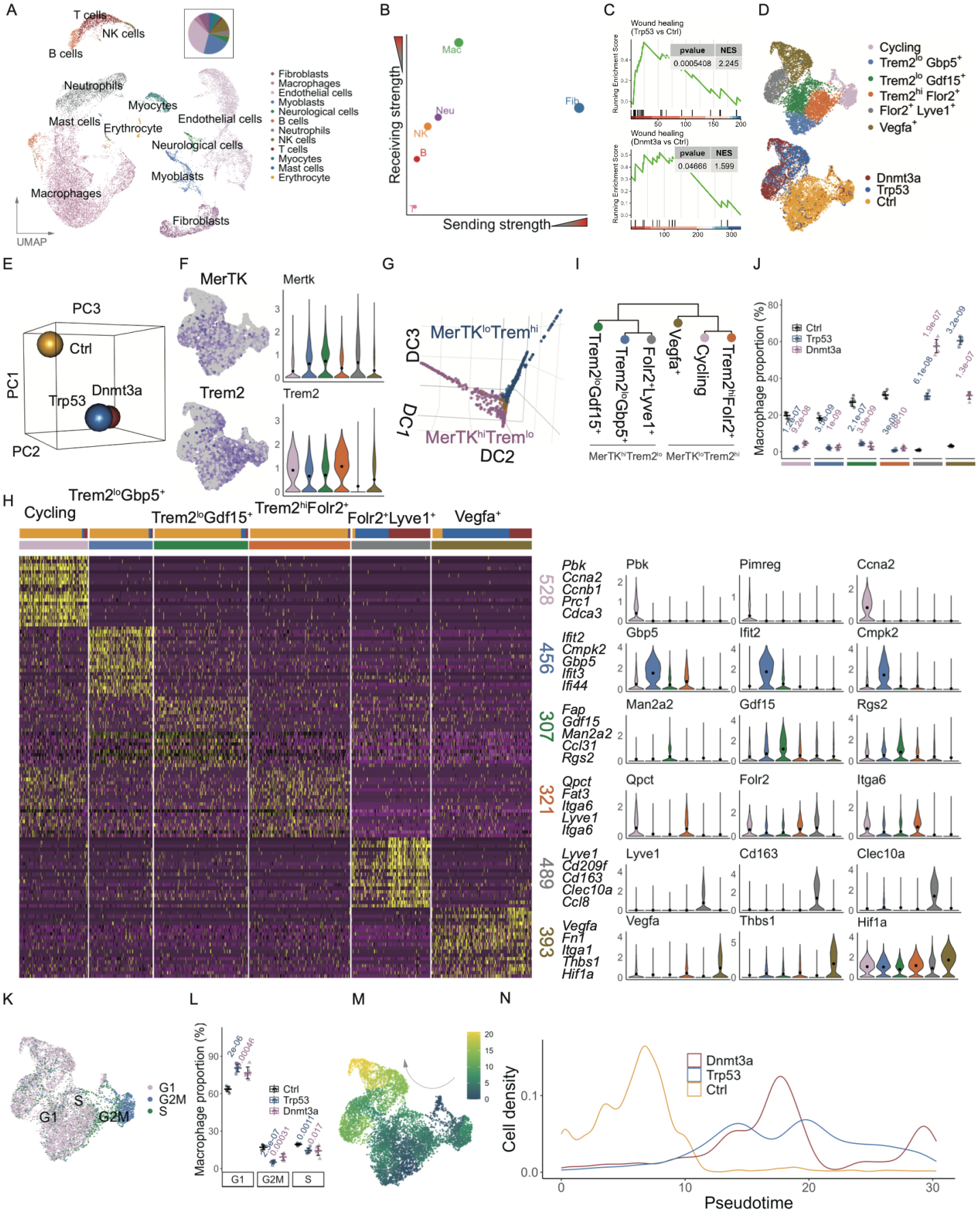

Figure 5. CH mice-derived macrophages exhibit enhanced tissue repair profile

A, Twelve cell clusters from muscle extracts after FAL in Uniform Manifold Approximation and Projection (UMAP) of 21,853 cells (n=6), annotated post hoc and colored by clustering.

B, Communication strength of each type of hematopoietic cells. Mac, macrophages; Endo, endothelial cells; Neu, neutrophils; T, T cells; Fib, fibroblasts; Mc, myocytes; Mb, myoblasts; B, B cells; NK, NK cells; Neuro, neuro system cells; Ery, erythrocytes; Mast, mast cells.

C, GSEA plot of wound healing gene signature in mutant vs. WT macrophages.

D, Six macrophage clusters in UMAP of 8,170 cells annotated post hoc and colored by clustering (top) or by cell origin (bottom).

E, PCA for mutant vs. WT macrophages.

F, MerTK and Trem2 expression in the 6 macrophage clusters.

G, Developmental relationship between clusters marked by MerTK and Trem2 expression.

H, Heatmap of the top 20 DEGs per cluster. Top cluster markers and the total number of genes characterized in each cluster are provided (left). Violin (right) plots representing expression level of macrophage cluster markers; medians marked by black dots and cluster identity by individual coloring.

I, Hierarchical clustering of macrophages.

J, Relative proportion of each clusters among macrophages from CH or Ctrl mice (n = 6). X-axis marks cluster identities individual coloring. mean±sd. P values are annotated. Student's t test.

K, Predicted cell cycle status of macrophages.

L, Relative proportion of each predicted cell cycle status among mutant vs. WT macrophages (n = 6). mean±sd. P values are annotated. Student's t test.

M, UMAP showing the macrophage differentiation trajectory with cells colored by pseudotime score.

N, Density plot showing the distribution of *Dnmt3a* CH, *Trp53* CH, or Ctrl mice-derived muscle cells through pseudotime.

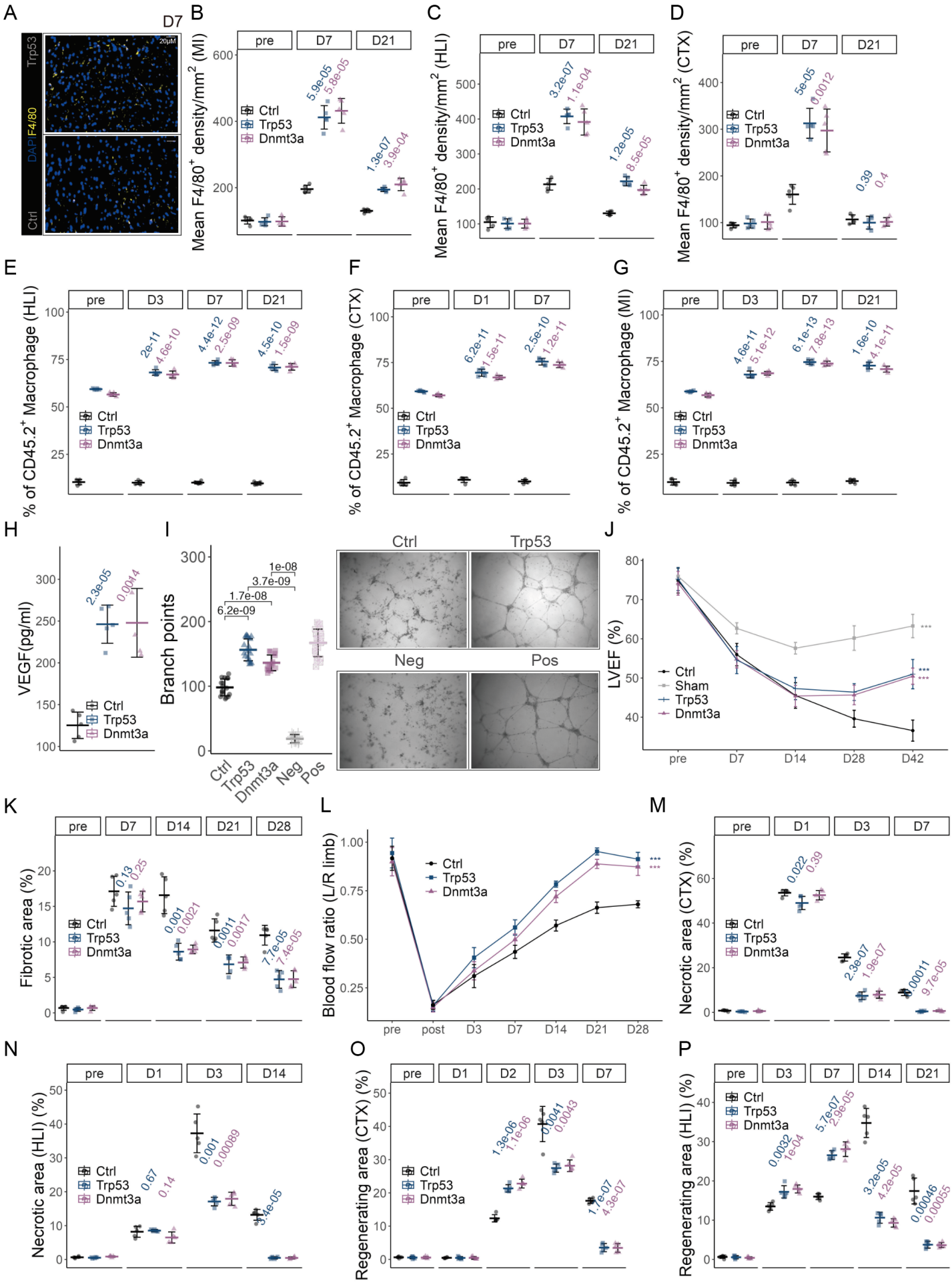
A
D7
Trp53
DAPI F4/80
Ctrl
20μM
B
Mean F4/80+ density/mm2 (MI)
pre
D7
D21
Ctrl
Trp53
Dnmt3a
5.9e-05
5.8e-05
1.3e-07
3.9e-04
C
Mean F4/80+ density/mm2 (HLI)
3.2e-07
1.1e-04
1.2e-05
8.5e-05
D
Mean F4/80+ density/mm2 (CTX)
5e-05
0.0012
0.39
0.4
E
% of CD45.2+ Macrophage (HLI)
pre
D3
D7
D21
2e-11
4.6e-10
4.4e-12
2.5e-09
4.5e-10
1.5e-09
F
% of CD45.2+ Macrophage (CTX)
pre
D1
D7
6.2e-11
1.5e-11
2.5e-10
1.2e-11
G
% of CD45.2+ Macrophage (MI)
pre
D3
D7
D21
4.6e-11
5.1e-12
6.1e-13
7.8e-13
1.6e-10
4.1e-11
H
VEGF(pg/ml)
2.3e-05
0.0014
I
Branch points
1e-08
3.7e-09
1.7e-08
6.2e-09
Ctrl
Trp53
Dnmt3a
Neg
Pos
J
LVEF (%)
Ctrl
Sham
Trp53
Dnmt3a
pre
D7
D14
D28
D42
K
Fibrotic area (%)
pre
D7
D14
D21
D28
0.13
0.25
0.001
0.0021
0.0011
0.0017
7.7e-05
7.4e-05
L
Blood flow ratio (L/R limb)
Ctrl
Trp53
Dnmt3a
pre
post
D3
D7
D14
D21
D28
M
Necrotic area (CTX) (%)
pre
D1
D3
D7
0.022
0.39
2.3e-07
1.9e-07
0.00011
9.7e-05
N
Necrotic area (HLI) (%)
pre
D1
D3
D14
0.67
0.14
0.001
0.00089
3.4e-05
O
Regenerating area (CTX) (%)
pre
D1
D2
D3
D7
1.3e-06
1.1e-06
0.0041
0.0043
1.7e-07
4.3e-07
P
Regenerating area (HLI) (%)
pre
D3
D7
D14
D21
0.0032
1e-04
5.7e-07
2.9e-05
3.2e-05
4.2e-05
0.00046
0.00055

Figure 6. *Trp53* and *Dnmt3a* mutant macrophages show fast expansion in response to injury and independently improve tissue repair

A, Representative images of macrophage density by F4/80 in the MI model. Scale bar: 20 μM.

B to C, Quantification of macrophage density by F4/80 in MI, HLI, and CTX models (n=5).

E to G, Quantification of mutant ($CD45.2^+$) macrophage fraction in flow cytometry in MI, HLI, and CTX models (n=5).

H, Quantification of VEGF level in the culture medium of macrophages isolated from WT, *Trp53* mutant, or *Dnmt3a* mutant mice after FAL (n=5).

I, Quantification and representative images from the endothelial cell assembly assay based on the number of intersecting branch points per field of view (×10) using macrophage conditioned medium. Data represent 5 fields of 3 independent replicates per condition (n = 15).

J, Quantification of left ventricular ejection fraction (LVEF) of WT mice transplanted with *Trp53*, *Dnmt3a*, or WT BMDMs after left anterior descending artery (LAD) ligation (n=10). Two-way ANOVA with post-hoc Tukey's multiple comparison tests.

K, Quantification of the fibrotic area of WT mouse heart transplanted with *Trp53*, *Dnmt3a*, or WT BMDMs after LAD ligation (n=5).

L, Quantification of hind limb blood flow of WT mice transplanted with *Trp53*, *Dnmt3a*, or WT BMDMs measured with laser Doppler perfusion imaging before ligation, immediately after FAL (n=5). pre, pre-ligation. post, immediately post-ligation. Two-way ANOVA with post-hoc Tukey's multiple comparison tests.

M and N, Quantification of muscle necrosis of WT mice transplanted with *Trp53*, *Dnmt3a*, or WT BMDMs in HLI and CTX models (n=5).

O and P, Quantification of regeneration area of WT mice transplanted with *Trp53*, *Dnmt3a*, or WT BMDMs in HLI and CTX models (n=5).

Graphs are mean±sd. In all figures, n refers to the number of mice unless noted. P values are annotated. pre, pre-ligation or pre-injection. Data are compared using Student's t test unless noted.

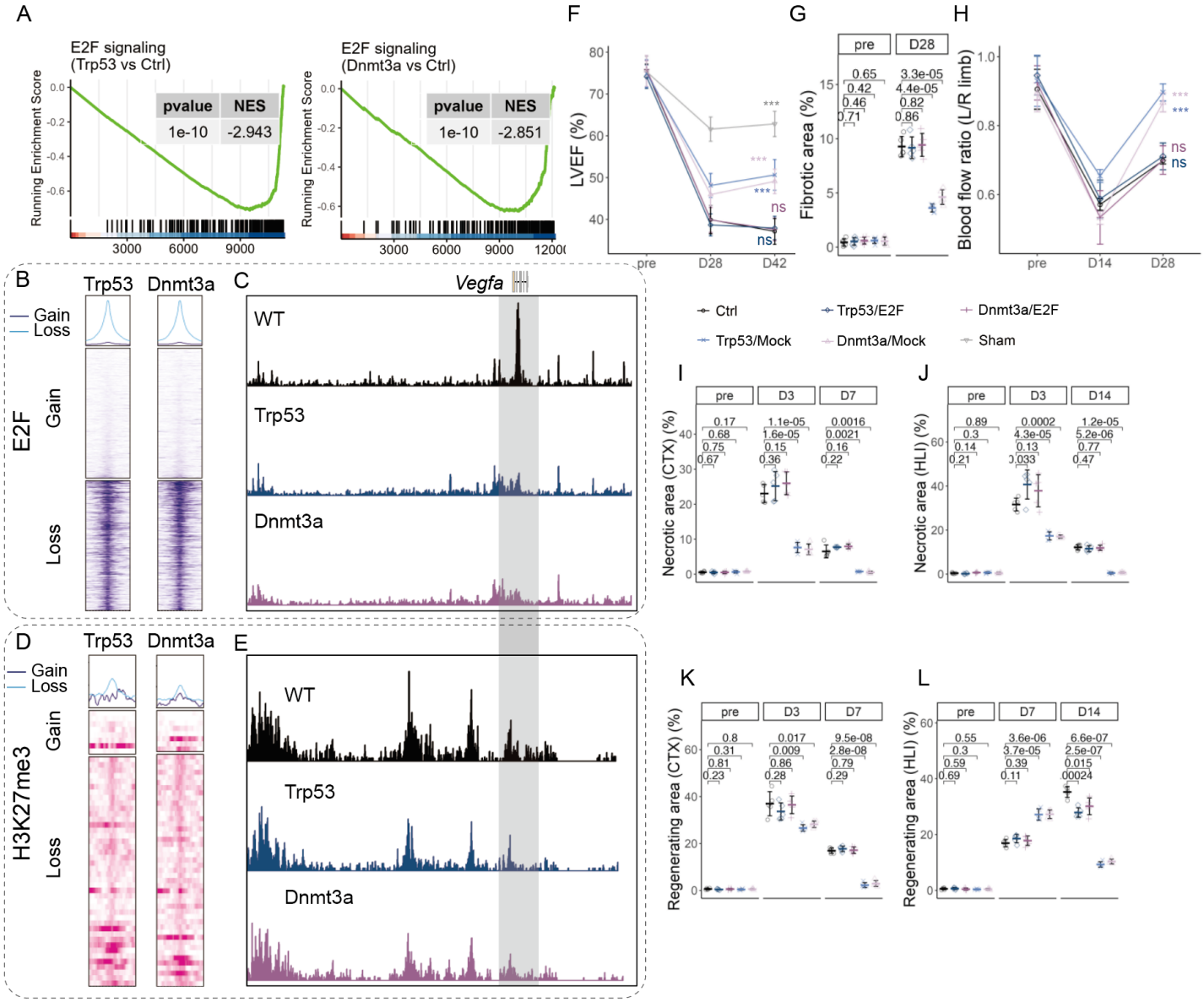

Figure 7. *Trp53* and *Dnmt3a* mutant macrophages accelerate tissue repair through E2F repression

A, GSEA plot of E2F signaling gene signature in mutant macrophages compared with WT macrophages.

B to E, Heatmaps and density plots of CUT&RUN profiling for E2F (B) and CUT&Tag for H3K27me3 (D) binding in *Trp53*- and *Dnmt3a*-mutant macrophages, stratified by genomic regions showing gain or loss of signal relative to WT controls. Genome browser tracks showing E2F (C) and H3K27me3 (D) binding signal at the Vegfa locus in *Trp53*- and *Dnmt3a*-mutant or WT macrophages.

F to L, Quantification of LVEF (F, n=10, two-way ANOVA with post-hoc Tukey's multiple comparison tests), fibrotic area (G), hind limb blood flow (H, two-way ANOVA with post-hoc Tukey's multiple comparison tests), muscle necrosis (I and J), and muscle regeneration area (K and L) after injury. n=5 unless noted.

Graphs are mean±sd. In all figures, n refers to the number of mice unless noted. P values are annotated. pre, pre-ligation or pre-injection. Data are compared using Student's t test unless noted.

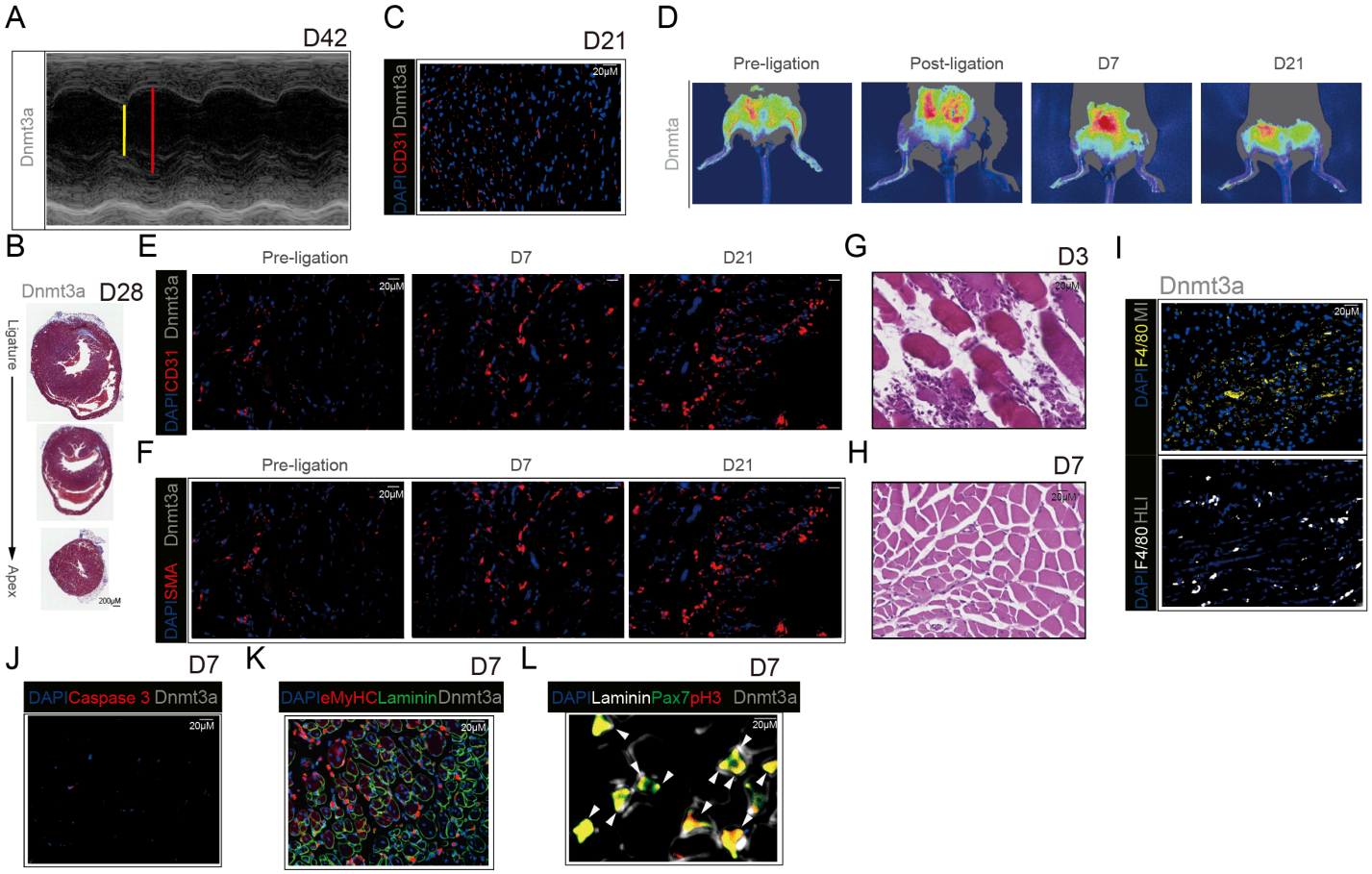

Figure S1. Representative images of *Dnmt3a* CH mice after tissue injury

A to L, Representative (*Dnmt3a*) image of M-mode echocardiography (A), fibrotic area by trichrome staining (B), and myocardium vasculature in the peri-infarct region (C) after LAD ligation; blood flow measured with laser Doppler perfusion imaging (D), CD31 staining to measure the capillary density (E), and smooth muscle α-actin (SMA) staining to measure the arteriole density (F) on ischemic limb muscle; necrosis area (G) and regenerating area (H) in CTX model; F4/80 staining to measure macrophage density in heart after LAD ligation and on ischemic limb muscle (I); caspase3 staining to measure muscle cell death (J), eMyHC staining to measure the early and late regenerating muscle fibers (K), and Pax7 and pH3 staining to measure the muscle satellite cells (L) in CTX model.

S2

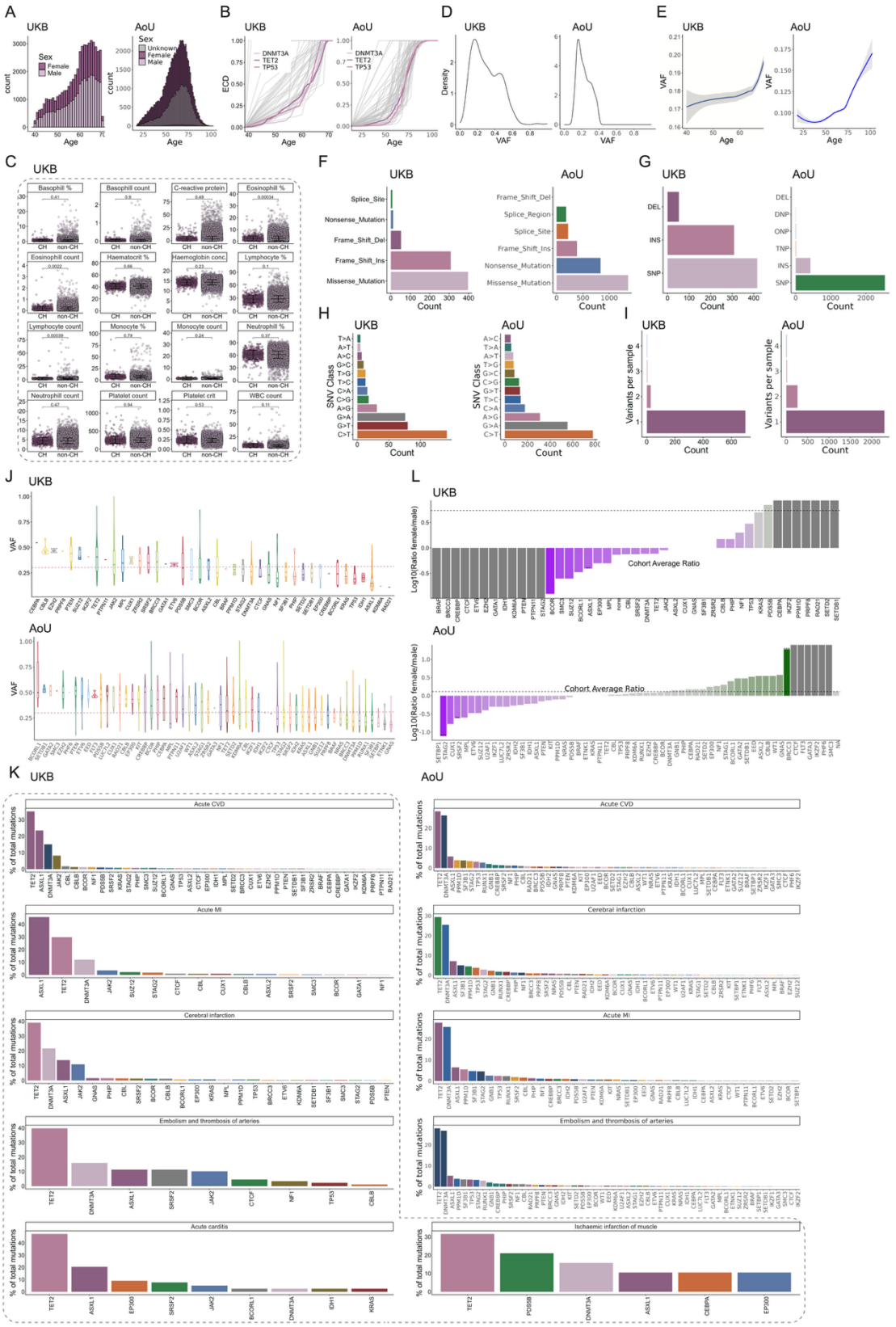
A
UKB
AoU
Sex
Female
Male
Unknown
count
Age
B
DNMT3A
TET2
TP53
ECD
D
Density
VAF
E
C
Basophil %
Basophil count
C-reactive protein
Eosinophil %
Eosinophil count
Haematocrit %
Haemoglobin conc
Lymphocyte %
Lymphocyte count
Monocyte %
Monocyte count
Neutrophil %
Neutrophil count
Platelet count
Platelet crit
WBC count
CH
non-CH
F
Splice_Site
Nonsense_Mutation
Frame_Shift_Del
Frame_Shift_Ins
Missense_Mutation
Count
G
DEL
INS
SNP
DNP
ONP
TNP
H
SNV Class
I
Variants per sample
J
L
Log10(Ratio female/male)
Cohort Average Ratio
K
% of total mutations
Acute CVD
Acute MI
Cerebral infarction
Embolism and thrombosis of arteries
Acute carditis
Ischaemic infarction of muscle

Figure S2. Characterization of acute cardiovascular disease patients in the UK Biobank and All of Us.

A, Histogram stratified by sex showing the age distribution of acute CVD individuals in the UKB cohort (n= 52,338) and AoU cohort (73,628).

B, Empirical cumulative distribution (ECD) of the age of individuals with CH stratified by the driver genes. TET2, DNMT3A, and TP53 are highlighted, and other CH genes are gray.

C, Blood count and lab results of CH vs non-CH individuals.

D, Density plot showing the variant allele fraction (VAF) distribution of all CH somatic mutations.

E, Clone size, estimated by the variant allele fraction (VAF), increases with age. The blue line represents the smoothed model fitted to a generalized additive model and the shadow represents the 95% CI.

F and G, Number of different variant types amongst the identified CH mutations.

H, Number of each of the six base substitution types amongst the identified CH mutations.

I, Number of individuals with 1, 2, 3, and 4 somatic mutations.

J, Violin plot summarizing the distribution of VAFs of mutations in 15,475 individuals with CH. The dashed line represents the VAF of the general cohort. Error bars are mean±sd.

K, CH-associated mutations in 61 analyzed genes that resulted in a variant allele fraction higher than 0.02 and remained positive after stringent unsupervised and supervised variant calling criteria were included and shown among patients with different types of acute CVDs.

L, Bar plot showing the female to male (F:M) ratio of CH carriers. The dashed vertical line shows the F:M ratio observed in the full cohort (F:M = 0.7). P values are from a chi-squared test comparing the distribution for each gene with non-CH individuals.

S3

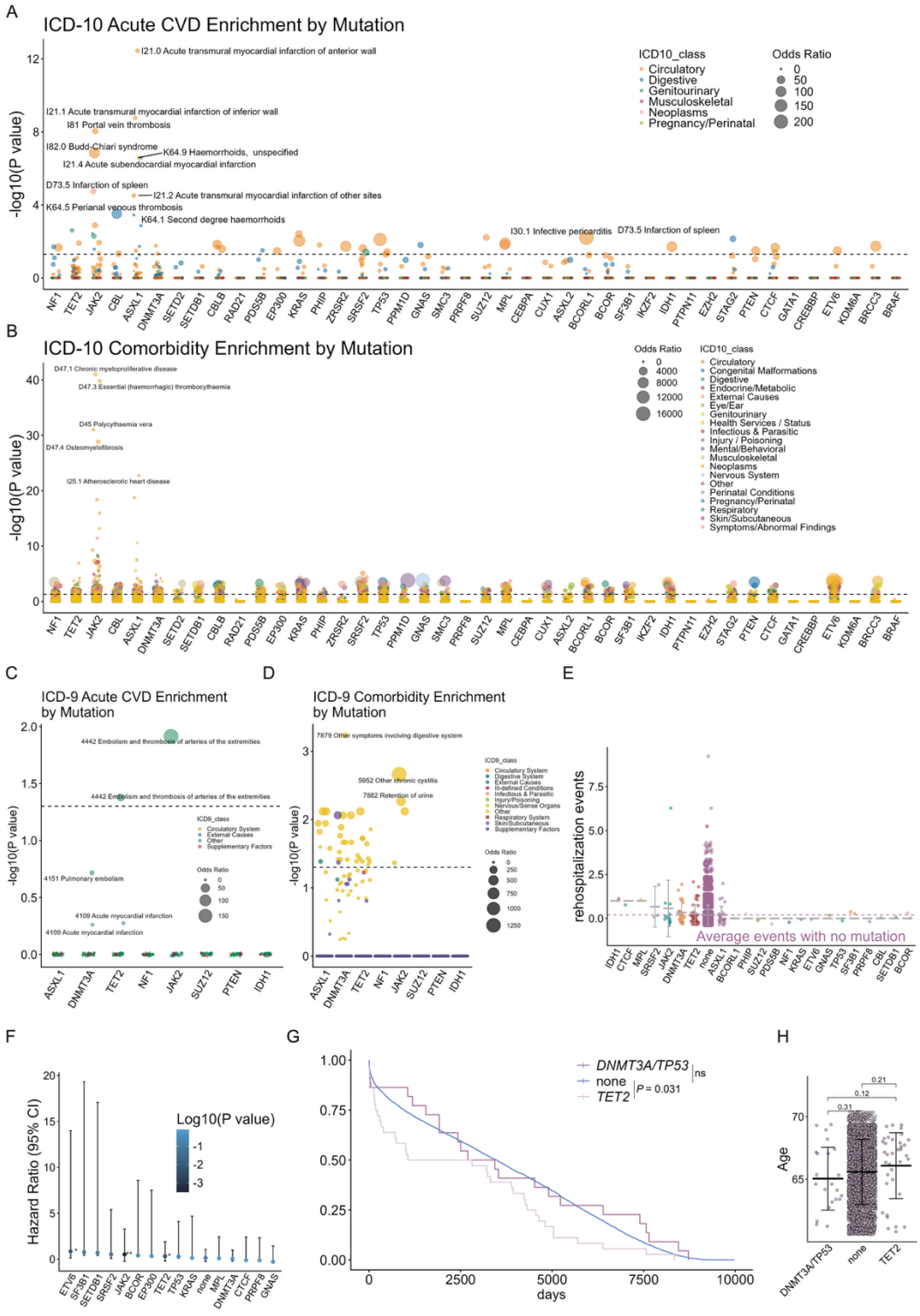
A
ICD-10 Acute CVD Enrichment by Mutation
-log10(P value)
I21.0 Acute transmural myocardial infarction of anterior wall
I21.1 Acute transmural myocardial infarction of inferior wall
I81 Portal vein thrombosis
I82.0 Budd-Chiari syndrome
K64.9 Haemorrhoids, unspecified
I21.4 Acute subendocardial myocardial infarction
D73.5 Infarction of spleen
I21.2 Acute transmural myocardial infarction of other sites
K64.5 Perianal venous thrombosis
K64.1 Second degree haemorrhoids
I30.1 Infective pericarditis
D73.5 Infarction of spleen
ICD10_class
Circulatory
Digestive
Genitourinary
Musculoskeletal
Neoplasms
Pregnancy/Perinatal
Odds Ratio
0
50
100
150
200
NF1 TET2 JAK2 CBL ASXL1 DNMT3A SETD2 SETDB1 CBLB RAD21 PDS5B EP300 KRAS PHIP ZRSR2 SRSF2 TP53 PPM1D GNAS SMC3 PRPF8 SUZ12 MPL CEBPA CUX1 ASXL2 BCORL1 BCOR SF3B1 IKZF2 IDH1 PTPN11 EZH2 STAG2 PTEN CTCF GATA1 CREBBP ETV6 KDM6A BRCC3 BRAF
B
ICD-10 Comorbidity Enrichment by Mutation
-log10(P value)
D47.1 Chronic myeloproliferative disease
D47.3 Essential (haemorrhagic) thrombocythaemia
D45 Polycythaemia vera
D47.4 Osteomyelofibrosis
I25.1 Atherosclerotic heart disease
Odds Ratio
0
4000
8000
12000
16000
ICD10_class
Circulatory
Congenital Malformations
Digestive
Endocrine/Metabolic
External Causes
Eye/Ear
Genitourinary
Health Services / Status
Infectious & Parasitic
Injury / Poisoning
Mental/Behavioral
Musculoskeletal
Neoplasms
Nervous System
Other
Perinatal Conditions
Pregnancy/Perinatal
Respiratory
Skin/Subcutaneous
Symptoms/Abnormal Findings
NF1 TET2 JAK2 CBL ASXL1 DNMT3A SETD2 SETDB1 CBLB RAD21 PDS5B EP300 KRAS PHIP ZRSR2 SRSF2 TP53 PPM1D GNAS SMC3 PRPF8 SUZ12 MPL CEBPA CUX1 ASXL2 BCORL1 BCOR SF3B1 IKZF2 IDH1 PTPN11 EZH2 STAG2 PTEN CTCF GATA1 CREBBP ETV6 KDM6A BRCC3 BRAF
C
ICD-9 Acute CVD Enrichment by Mutation
-log10(P value)
4442 Embolism and thrombosis of arteries of the extremities
4442 Embolism and thrombosis of arteries of the extremities
4151 Pulmonary embolism
4109 Acute myocardial infarction
4109 Acute myocardial infarction
ICD9_class
Circulatory System
External Causes
Other
Supplementary Factors
Odds Ratio
0
50
100
150
ASXL1 DNMT3A TET2 NF1 JAK2 SUZ12 PTEN IDH1
D
ICD-9 Comorbidity Enrichment by Mutation
-log10(P value)
7879 Other symptoms involving digestive system
5952 Other chronic cystitis
7882 Retention of urine
ICD9_class
Circulatory System
Digestive System
External Causes
Ill-defined Conditions
Infectious & Parasitic
Injury/Poisoning
Nervous/Sense Organs
Other
Respiratory System
Skin/Subcutaneous
Supplementary Factors
Odds Ratio
0
250
500
750
1000
1250
ASXL1 DNMT3A TET2 NF1 JAK2 SUZ12 PTEN IDH1
E
rehospitalization events
Average events with no mutation
IDH1 CTCF MPL SRSF2 JAK2 DNMT3A TET2 none ASXL1 BCORL1 PHIP SUZ12 PDS5B NF1 KRAS ETV6 GNAS TP53 SF3B1 PRPF8 CBL SETDB1 BCOR
F
Hazard Ratio (95% CI)
Log10(P value)
-1
-2
-3
ETV6 SF3B1 SETDB1 SRSF2 JAK2 BCOR EP300 TET2 TP53 KRAS none MPL DNMT3A CTCF PRPF8 GNAS
G
DNMT3A/TP53
none
TET2
ns
P = 0.031
days
H
Age
0.21
0.12
0.31
DNMT3A/TP53
none
TET2

Figure S3. Distinct prognosis of acute cardiovascular disease patients with clonal hematopoiesis.

A, Phenome-wide association study of CH and incident acute cardiovascular disease (CVD) outcomes. Phenotypes were extracted from the International Classification of Diseases version-10 (ICD-10) disease codes and grouped into different categories. A total of 50 acute CVD ICD-10 codes (listed in methods) were tested using logistic regression. The odds ratio (OR) of each code is represented by a single point with a size scale. The black dashed line represents the phenome-wide significant P-value threshold of 0.05. Full results with ORs, 95% confidence intervals (CIs), P-values and FDRs are reported in Supplementary Table 1.

B, Phenome-wide association study of CH and incident comorbidities outcomes. Phenotypes were extracted from the International Classification of Diseases version-10 (ICD-10) disease codes and grouped into different categories. A total of 9,182 non-acute cardiovascular disease ICD-10 codes were identified using logistic regression. The odds ratio (OR) of each code is represented by a single point with a size scale. The black dashed line represents the phenome-wide significant P-value threshold of 0.05. Full results with ORs, 95% confidence intervals (CIs), P-values and FDRs are reported in Supplementary Table 1.

C, Phenome-wide association study of CH and incident disease outcomes. Phenotypes were extracted from the International Classification of Diseases version-9 (ICD-9) disease codes and grouped into different categories. A total of 31 acute cardiovascular disease ICD-9 codes were identified using logistic regression. The odds ratio (OR) of each code is represented by a single point with a size scale. The black dashed line represents the phenome-wide significant P-value threshold of 0.05. Full results with ORs, 95% confidence intervals (CIs), P-values and FDRs are reported in Supplementary Table 2.

D, Phenome-wide association study of CH and incident disease outcomes. Phenotypes were extracted from the International Classification of Diseases version-9 (ICD-9) disease codes and grouped into different categories. A total of 1,509 non-acute cardiovascular disease ICD-9 codes were identified using logistic regression. The odds ratio (OR) of each code is represented by a single point with a size scale. The black dashed line represents the phenome-wide significant P-value threshold of 0.05. Full results with ORs, 95% confidence intervals (CIs), P-values and FDRs are reported in Supplementary Table 2.

E, Rehospitalization events of acute CVD patients carrying each CH mutation. Dashed line reflects the incidence of rehospitalization for patients who were not carriers of CH.

F, Effect of CH mutations on the survival outcomes of acute CVD. HR, 95% CI and two-sided Wald P value were calculated from the Cox proportional-hazards model.

G, Overall survival of patients with *TET2*, *DNMT3A* or *TP53*, or without mutations. n = 22 (*DNMT3A=20*/*TP53=2*), 36 (*TET2*), and 5,148 (none). P values are for log-rank tests.

H, Age distribution between groups of *TET2*, *DNMT3A* or *TP53*, or without mutations. Error bars are mean±sd. Student's t test.

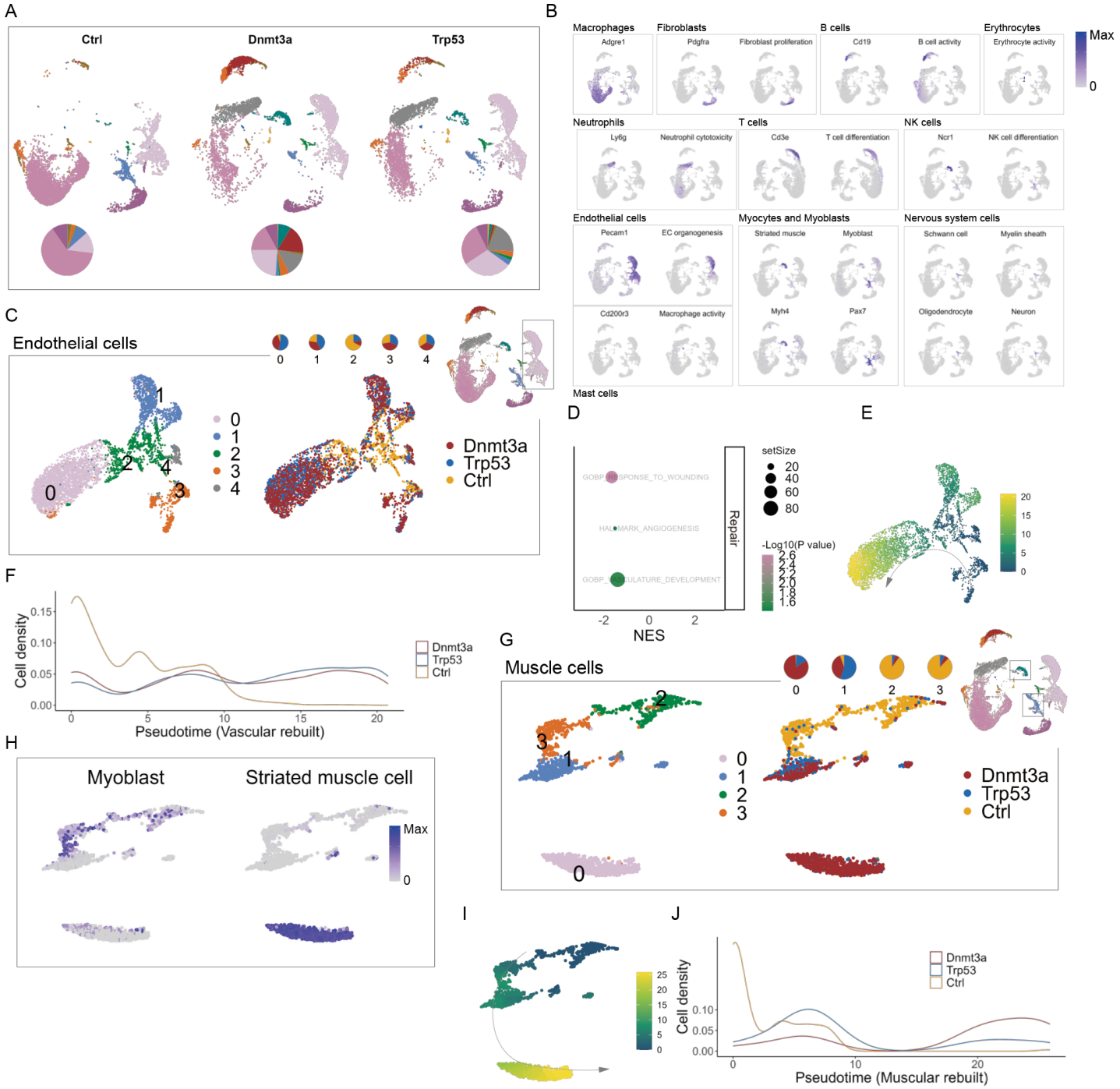

Figure S4. scRNA-seq reveals more differentiated tissue cell populations in CH mice

A, Cell distribution of *Dnmt3a* CH, *Trp53* CH, or Ctrl mice-derived cells.

B, Expression (color bar) of key cell-type marker genes and gene signatures.

C, Five endothelial cell clusters in UMAP of 4,820 cells in the endothelial cell subset, as colored by clustering (left) or by cell origin (right). The pie chart represents the portion of *Dnmt3a* CH, *Trp53* CH, or Ctrl mice-derived cells in each cluster.

D, Dot plot of gene set enrichment analysis (GSEA) showing the biological process of cluster 0 versus other clusters. Shown GSESA gene signatures are GOBP_VASCULATURE_DEVELOPMENT, HALLMARK_ANGIOGENESIS, and GOBP_RESPONSE_TO_WOUNDING. P values are annotated with a colored scheme. NES, normalized enrichment score.

E, UMAP showing the endothelial cell differentiation trajectory with cells colored by pseudotime score.

F, Density plot showing the distribution of *Dnmt3a* CH, *Trp53* CH, or Ctrl mice-derived endothelial cells through pseudotime.

G, Three muscle cell clusters in UMAP of 1,646 cells in the muscular cell subset, as colored by clustering (left) or by cell origin (right). The pie chart represents the portion of *Dnmt3a* CH, *Trp53* CH, or Ctrl mice-derived cells in each cluster.

H, The expression level of myoblast (GOBP_REGULATION_OF_MYOBLAST_PROLIFERATION) or striated muscle cell (GOBP_STRIATED_MUSCLE_CELL_DEVELOPMENT) gene signatures among muscle cell clusters.

I, UMAP showing the muscle cell differentiation trajectory with cells colored by pseudotime score.

J, Density plot showing the distribution of *Dnmt3a* CH, *Trp53* CH, or Ctrl mice-derived muscle cells through pseudotime.

S5

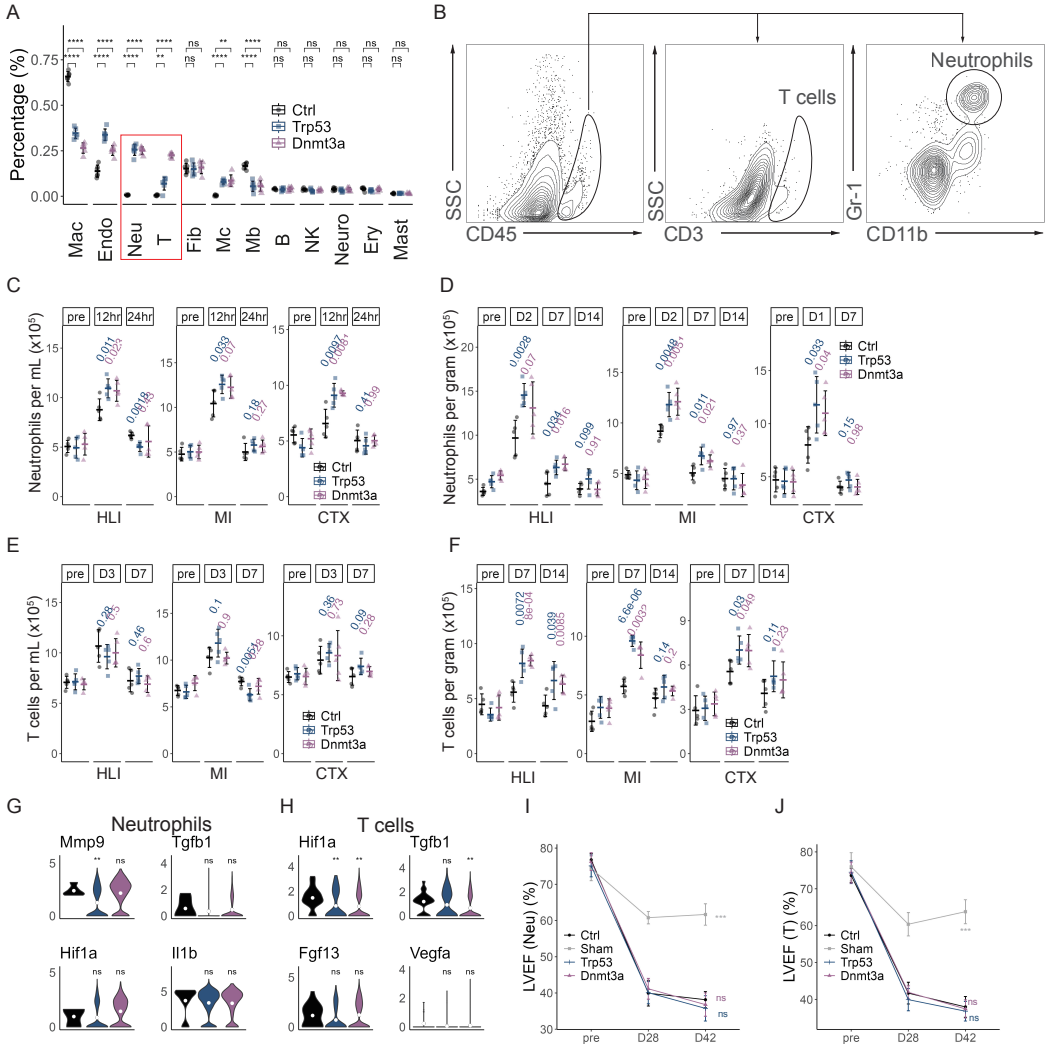
A
Percentage (%)
Ctrl
Trp53
Dnmt3a
Mac
Endo
Neu
T
Fib
Mc
Mb
B
NK
Neuro
Ery
Mast
B
SSC
CD45
CD3
Gr-1
CD11b
T cells
Neutrophils
C
Neutrophils per mL (x10^5)
pre
12hr
24hr
HLI
MI
CTX
D
Neutrophils per gram (x10^5)
D2
D7
D14
D1
E
T cells per mL (x10^5)
D3
F
T cells per gram (x10^5)
G
Neutrophils
Mmp9
Tgfb1
Hif1a
Il1b
H
T cells
Hif1a
Tgfb1
Fgf13
Vegfa
I
LVEF (Neu) (%)
Sham
pre
D28
D42
J
LVEF (T) (%)

Figure S5 . T cell and neutrophil expansion are increased in the peripheral blood and injured tissue of CH mice but do not independently improve cardiac repair

A, Quantification of the percentage of *Dnmt3a* CH, *Trp53* CH, or Ctrl mice-derived cells among each type of cells. Mac, macrophages; Endo, endothelial cells; Neu, neutrophils; T, T cells; Fib, fibroblasts; Mc, myocytes; Mb, myoblasts; B, B cells; NK, NK cells; Neuro, neuro system cells; Ery, erythrocytes; Mast, mast cells.

B, Gating strategy of identifying neutrophils and T cells in flow cytometry.

C and D, Quantification of absolute numbers of peripheral neutrophils after FAL and tissue local neutrophils in HLI, MI, and CTX models (n=5).

E and F, Quantification of absolute numbers of peripheral T cells after FAL and tissue local T cells in HLI, MI, and CTX models (n=5).

G and H, Individual cell expression (L and N) of pro-angiogenic factors in neutrophils (K and L) and T cells (M and N).

I and J, Quantification of left ventricular ejection fraction (LVEF) of CH or Ctrl mice after left anterior descending artery (LAD) ligation and neutrophils (K) or T cells (L) transplantation (n=10). Two-way ANOVA with post-hoc Tukey's multiple comparison tests.

Graphs are mean±sd. In all figures, n refers to the number of mice unless noted. P values are annotated. pre, pre-ligation or pre-injection. Data are compared using Student's t test unless noted.

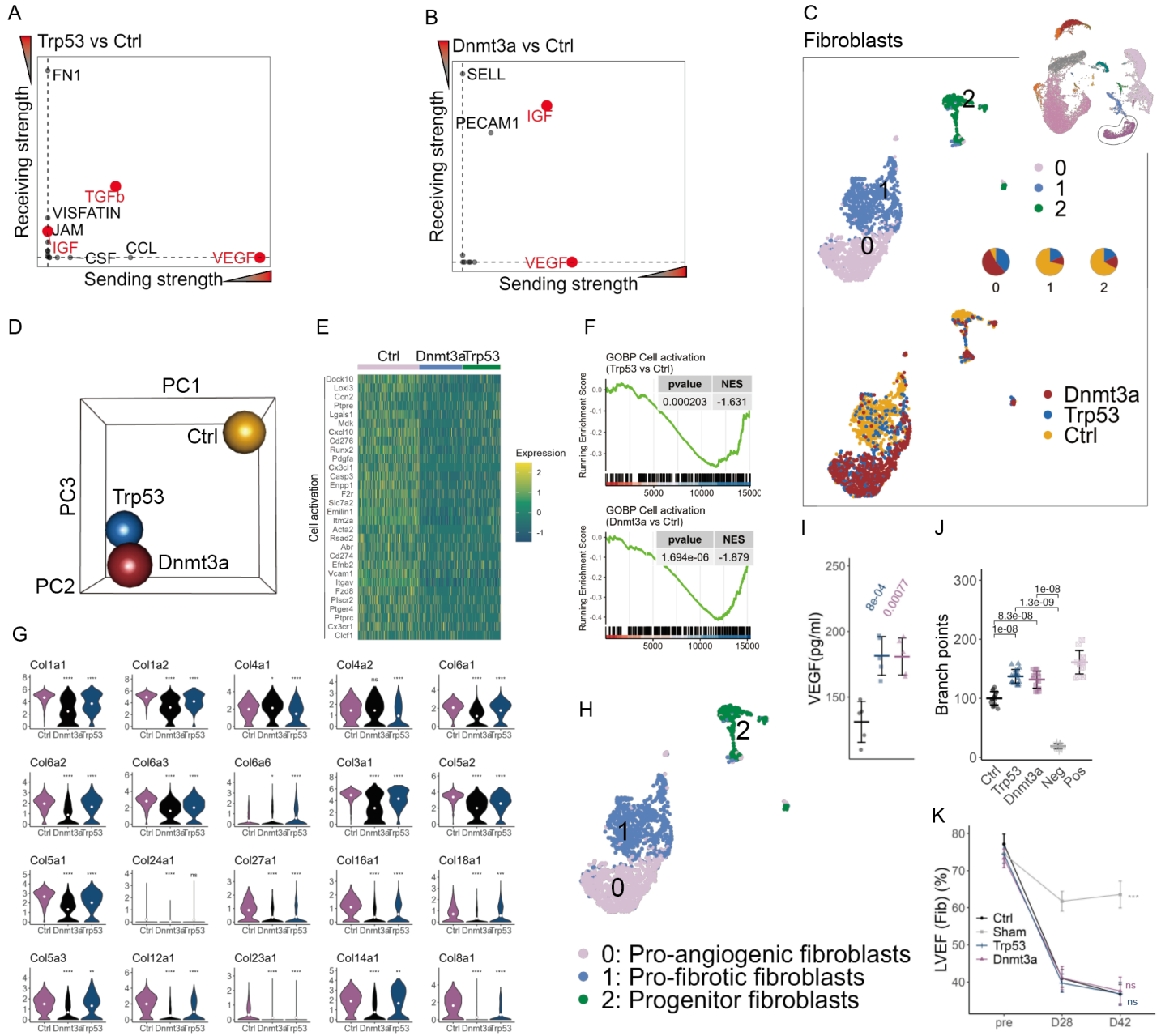

Figure S6. CH mice-derived fibroblasts are skewed toward a pro-angiogenic state

A and B, Change of signaling strength in CH mice-derived fibroblasts compared with Ctrl mice-derived fibroblasts.

C, Three fibroblast clusters in UMAP of 1,852 cells colored by clustering (top) or by cell origin (bottom). The pie chart represents the portion of *Dnmt3a* CH, *Trp53* CH, or Ctrl mice-derived cells in each cluster.

D, Principal component analysis (PCA, E) and Pearson distance tree (F) for *Dnmt3a* CH, *Trp53* CH, or Ctrl mice-derived fibroblasts.

E, Heatmap of genes associated with cell activation across *Dnmt3a* CH, *Trp53* CH, or Ctrl mice-derived fibroblasts.

F, GSEA plot of GOBP cell activation gene signature in *Dnmt3a* CH or *Trp53* CH compared with Ctrl mice-derived fibroblasts.

G, Violin plot showing the expression level of pro-fibrotic genes in CH and Ctrl mice-derived fibroblasts.

H, Post hoc annotated fibroblasts.

I, Quantification of VEGF level in the culture medium of fibroblasts isolated from WT, Trp53 mutant, or Dnmt3a mutant mice (n=5).

J, Quantification from the endothelial cell assembly assay based on the number of intersecting branch points per field of view (×10) using fibroblast conditioned medium. Data represent 5 fields of 3 independent replicates per condition (n = 15).

K, Quantification of left ventricular ejection fraction (LVEF) of mice after left anterior descending artery (LAD) ligation and transplanted with fibroblasts isolated from WT or *Trp53* or *Dnmt3a* mutant mice. Two-way ANOVA with post-hoc Tukey's multiple comparison tests.

Graphs are mean±sd. In all figures, n refers to the number of mice unless noted. P values are annotated. Data are compared using Student's t test unless noted.

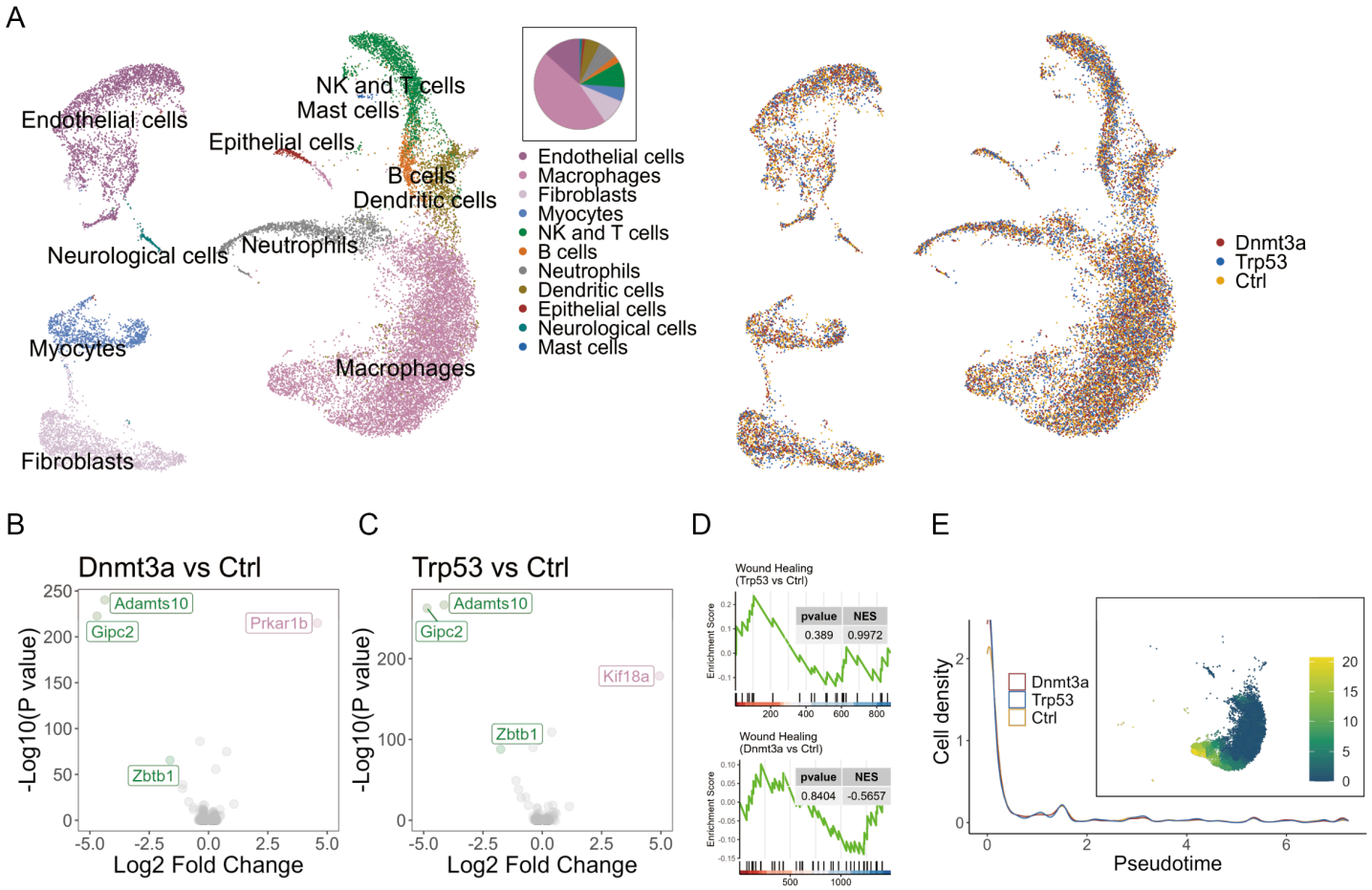

Figure S7. Baseline transcriptional profile of hematopoietic and tissue cells from CH and Ctrl mice hind limb

A, Eleven cell clusters from muscle extracts without injury in UMAP of 22,443 cells pooled from two mice of each condition, annotated post hoc and colored by clustering (left) or condition (right).

B and C, Volcano plot showing the relative expression level of DEGs in mutant vs. WT macrophages.

D, GSEA plot of wound healing gene signature in mutant vs. WT macrophages.

E, Density plot showing the distribution of mutant vs. WT macrophages through pseudotime. Inset, UMAP shows the macrophage differentiation trajectory with cells colored by pseudotime score.

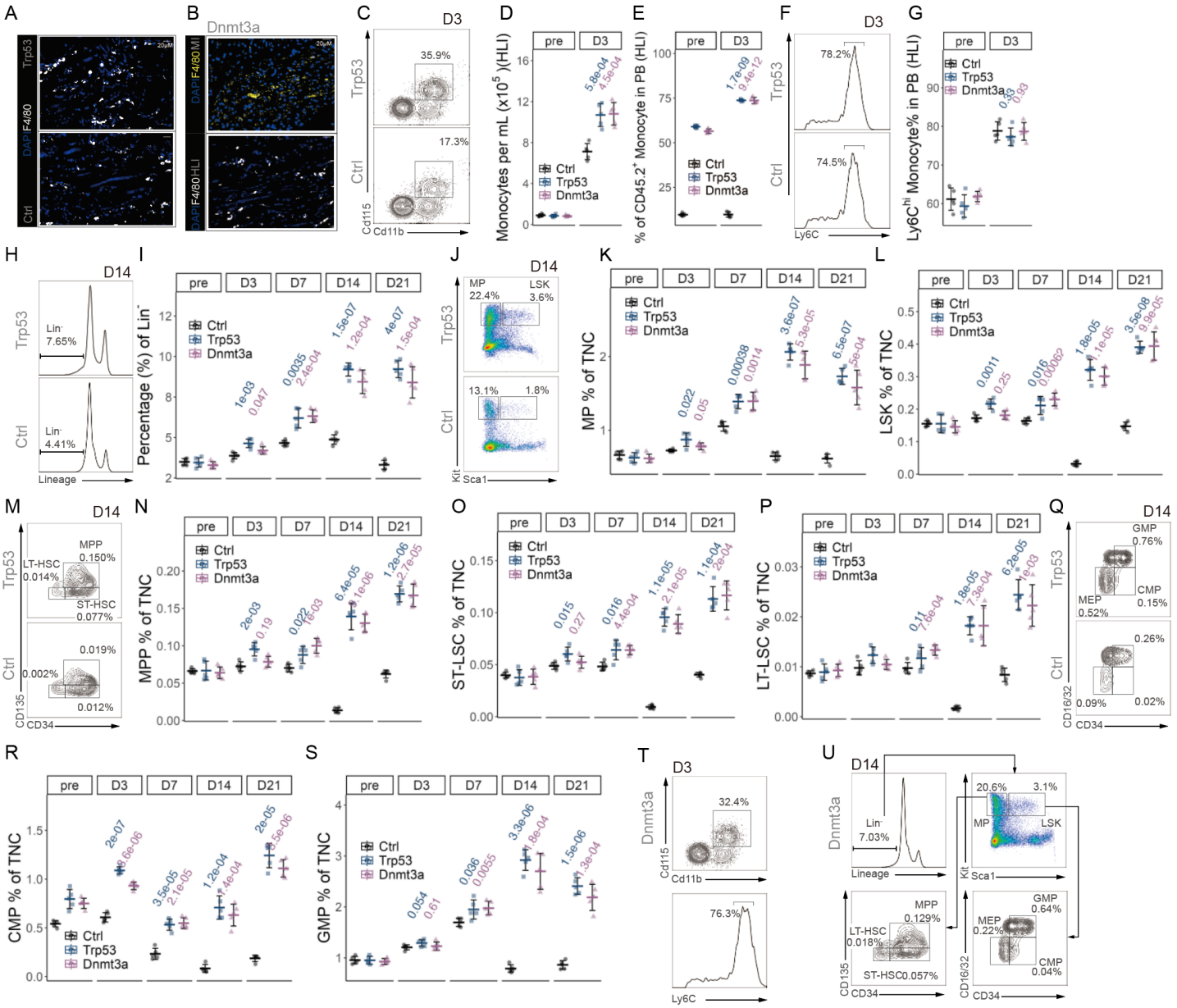

Figure S8. Clonal hematopoiesis mice exhibit persistent HSPC expansion and myeloid lineage bias in response to ischemic injury

A, Representative images of macrophage density in *Trp53* CH and Ctrl mice by F4/80 in HLI model (n=5), Scale bar: 20 μM.

B, Representative images of macrophage density in *Dnmt3a* CH mice by F4/80 in MI and HLI model (n=5), Scale bar: 20 μM.

C and D, Representative images and quantification of peripheral monocytes absolute number in flow cytometry after FAL (n=5).

E, Quantification of peripheral mutant (CD45.2^{+}) monocytes fraction in flow cytometry after FAL (n=5).

F and G, Representative images and quantification of peripheral Ly6C^{hi} monocytes percentage in flow cytometry after FAL (n=5).

H and I, Representative images and quantification of Lin^{-} cells in flow cytometry after FAL (n=5).

J to L, Representative images and quantification of myeloid progenitors and LSK cells in total nucleated cells (TNCs) in flow cytometry after FAL (n=5).

M to P, Representative images and quantification of percentage of multipotent progenitors (MPP), short-term hematopoietic stem cells (ST-HSC), and long-term HSCs (LT-HSC) in TNCs in flow cytometry after FAL (n=5).

Q to S, Representative images and quantification of percentage of common myeloid progenitors (CMP), megakaryocyte-erythroid progenitors (MEP), and granulocyte-monocyte progenitors (GMP) in total nucleated cells (TNCs) in flow cytometry after FAL (n=5).

T, Representative images of monocytes in the PB 3 days after FAL in *Dnmt3a* CH mice.

U, Representative images and gating strategy of HSPCs in the BM 14 days after FAL in *Dnmt3a* CH mice.

Graphs are mean±sd. In all figures, n refers to the number of mice unless noted. P values are annotated. pre, pre-ligation. Data are compared using Student's t test unless noted.

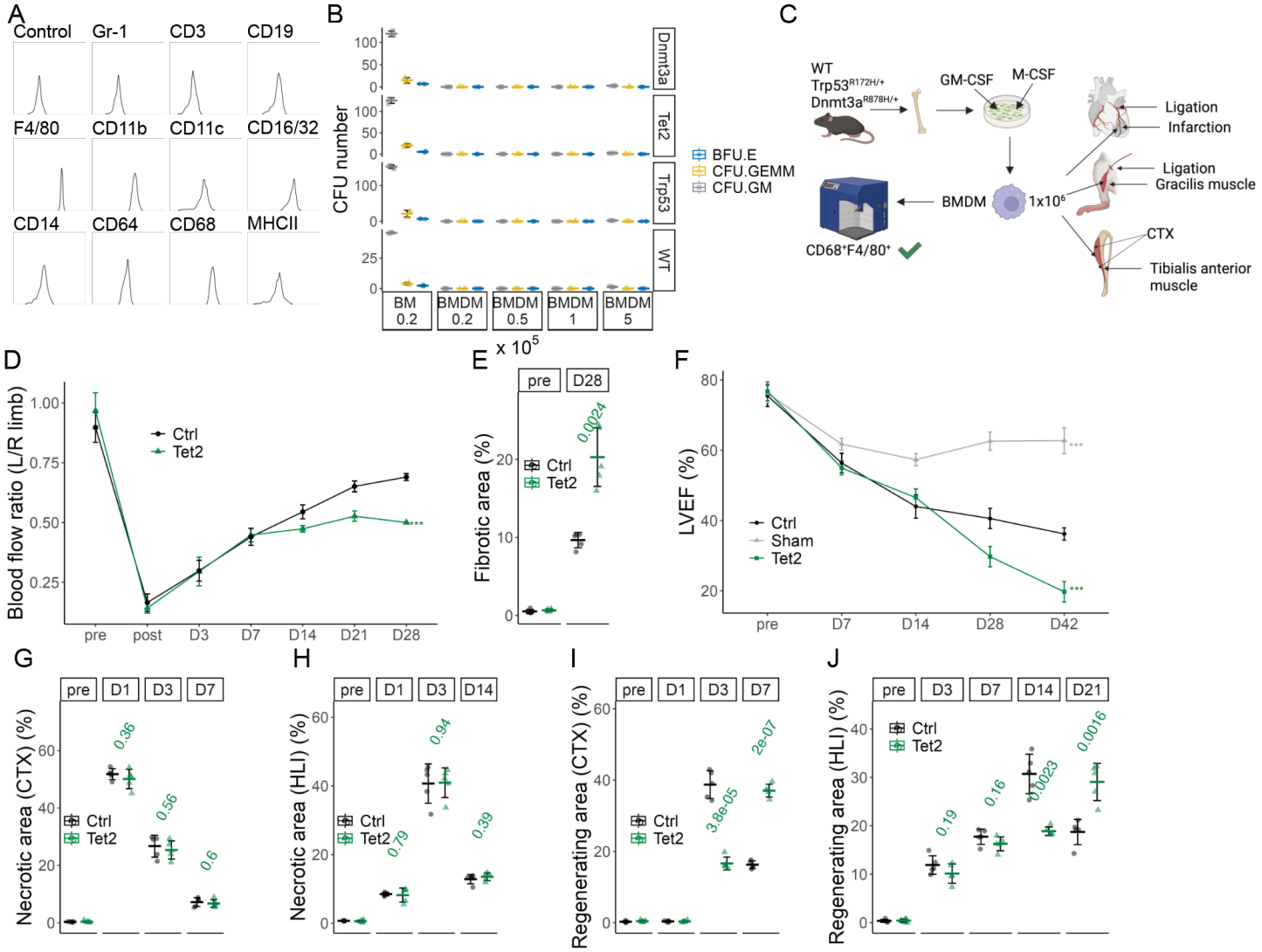

Figure S9. Baseline transcriptional profile of hematopoietic and tissue cells from CH and Ctrl mice hind limb

A, Representative image of flow cytometry evaluation of cell-surface phenotypic markers on mutant BMDMs before transplantation.

B, Colony counts of BFU-E, CFU-GEMM and CFU-GM from BMDMs (n = 3).

C, Schematic diagram of BMDM injection.

D, Quantification of left ventricular ejection fraction (LVEF) of WT mice transplanted with *Tet2* KO or WT BMDMs after left anterior descending artery (LAD) ligation (n=10). Two-way ANOVA with post-hoc Tukey's multiple comparison tests.

E, Quantification of the fibrotic area of WT mouse heart transplanted with *Tet2* KO or WT BMDMs after LAD ligation (n=5).

F, Quantification of hind limb blood flow of WT mice transplanted with *Tet2* KO or WT BMDMs measured with laser Doppler perfusion imaging before ligation, immediately after FAL (n=5). pre, pre-ligation. post, immediately post-ligation. Two-way ANOVA with post-hoc Tukey's multiple comparison tests.

G and H, Quantification of muscle necrosis of WT mice transplanted with *Tet2* KO or WT BMDMs in HLI and CTX models (n=5).

I and J, Quantification of regeneration area of WT mice transplanted with *Tet2* KO or WT BMDMs in HLI and CTX models (n=5).

Graphs are mean±sd. In all figures, n refers to the number of mice unless noted. P values are annotated. pre, pre-ligation or pre-injection. Data are compared using Student's t test unless noted.

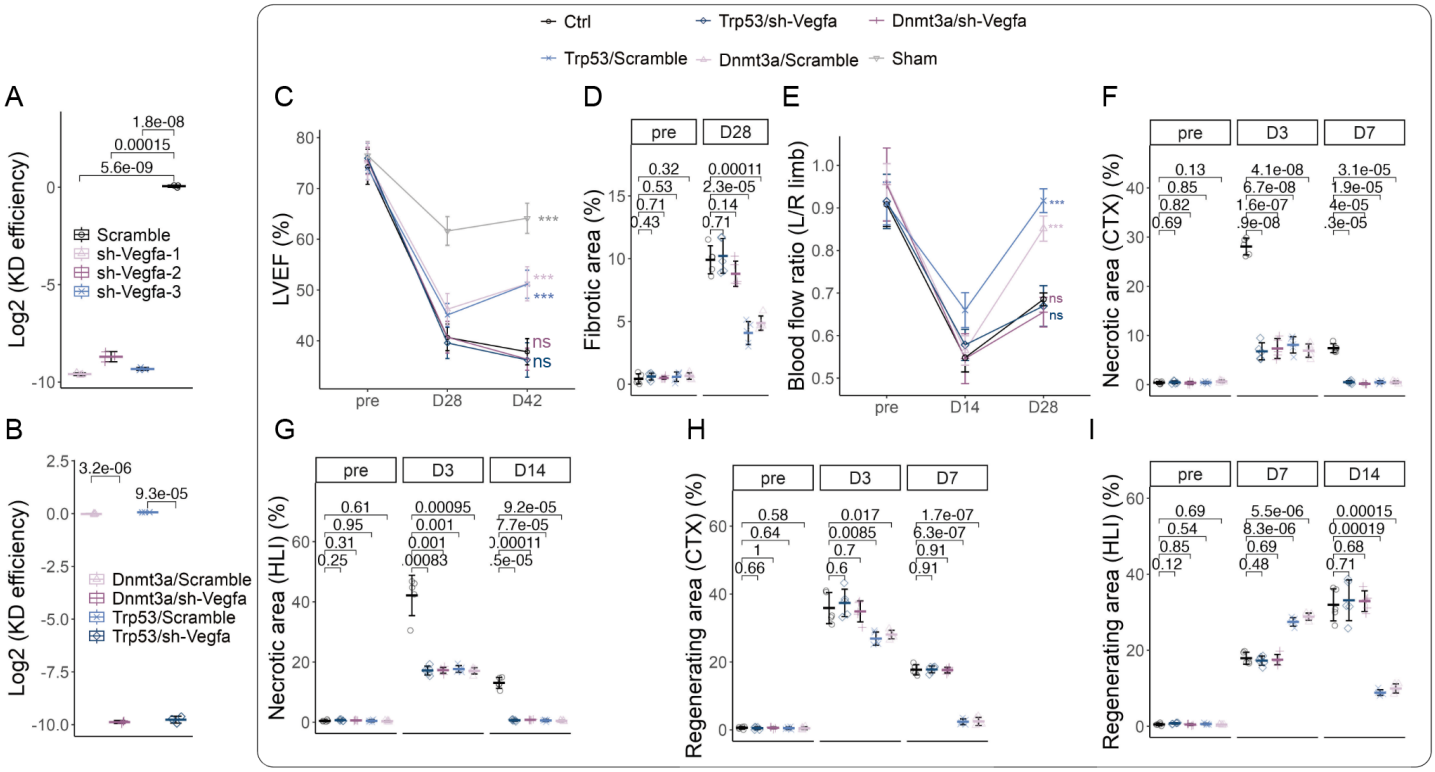

Figure S10. VEGF knockdown in mutant macropages rescued the accelerated tissue repair phenotype

A, KD efficiency of three sh-RNAs of *Vegfa* and Scramble quantified by qRT-PCR and divided by non-infected control (n=3) in WT BMDMs.

B, KD efficiency of sh-RNA-1 in *Trp53* or *Dnmt3a* mutant macrophages quantified by qRT-PCR and divided by non-infected *Trp53* or *Dnmt3a* mutant macrophages (n=3).

C, Quantification of left ventricular ejection fraction (LVEF) of WT mice transplanted with *Trp53* or *Dnmt3a* with VEGF KD or scramble, or WT BMDMs after left anterior descending artery (LAD) ligation (n=10). Two-way ANOVA with post-hoc Tukey's multiple comparison tests.

D, Quantification of the fibrotic area of WT mouse heart transplanted with *Trp53* or *Dnmt3a* with VEGF KD or scramble, or WT BMDMs after LAD ligation (n=5).

E, Quantification of hind limb blood flow of WT mice transplanted with *Trp53* or *Dnmt3a* with VEGF KD or scramble, or WT BMDMs measured with laser Doppler perfusion imaging before ligation, immediately after FAL (n=5). pre, pre-ligation. post, immediately post-ligation. Two-way ANOVA with post-hoc Tukey's multiple comparison tests.

F and G, Quantification of muscle necrosis of WT mice transplanted with *Trp53* or *Dnmt3a* with VEGF KD or scramble, or WT BMDMs in HLI and CTX models (n=5).

H and I, Quantification of regeneration area of WT mice transplanted with *Trp53* or *Dnmt3a* with VEGF KD or scramble, or WT BMDMs in HLI and CTX models (n=5).

Graphs are mean±sd. In all figures, n refers to the number of mice unless noted. P values are annotated. pre, pre-ligation or pre-injection. Data are compared using Student's t test unless noted.

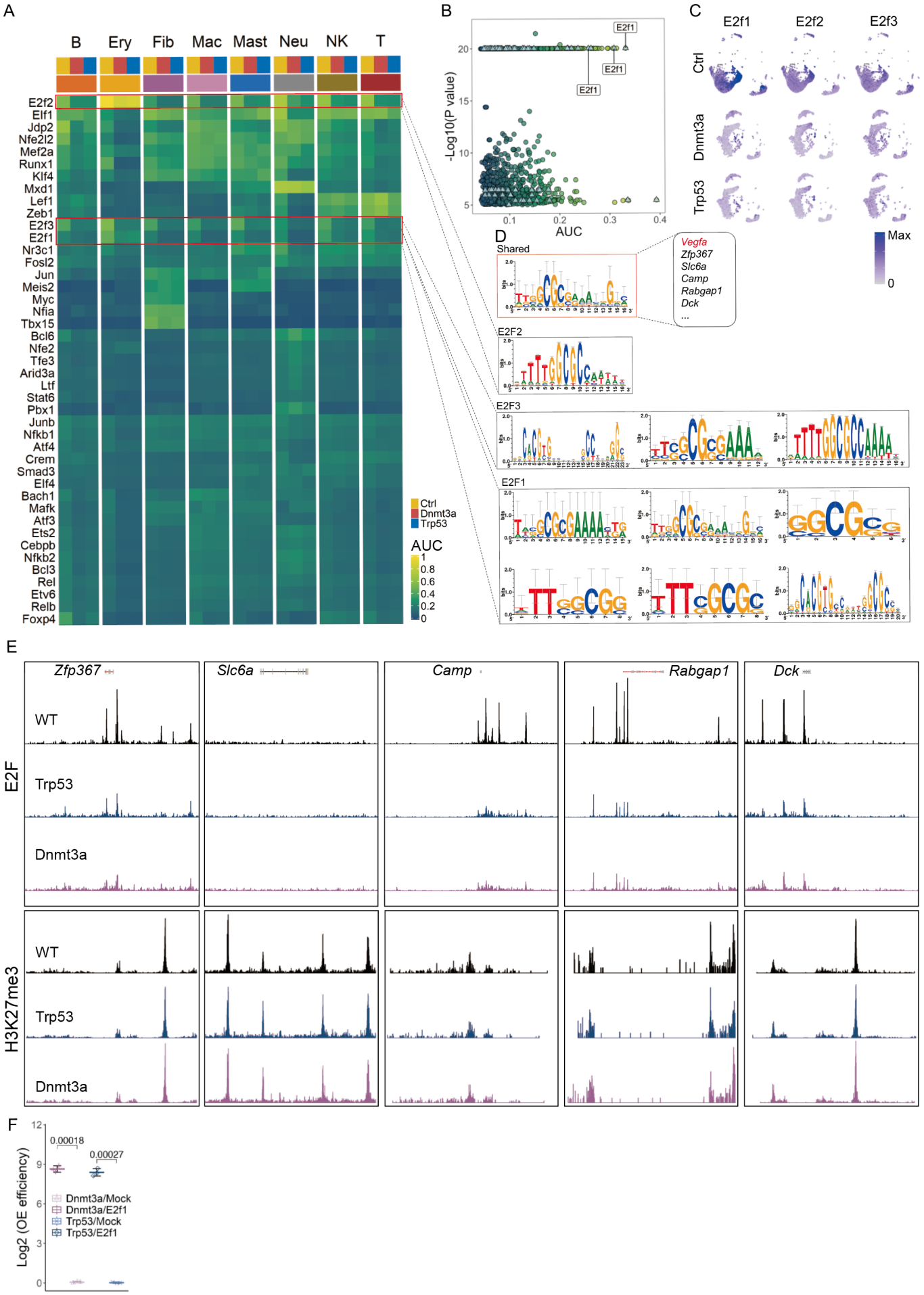
A
B
Ery
Fib
Mac
Mast
Neu
NK
T
E2f2
Elf1
Jdp2
Nfe2l2
Mef2a
Runx1
Klf4
Mxd1
Lef1
Zeb1
E2f3
E2f1
Nr3c1
Fosl2
Jun
Meis2
Myc
Nfia
Tbx15
Bcl6
Nfe2
Tfe3
Arid3a
Ltf
Stat6
Pbx1
Junb
Nfkb1
Atf4
Crem
Smad3
Elf4
Bach1
Mafk
Atf3
Ets2
Cebpb
Nfkb2
Bcl3
Rel
Etv6
Relb
Foxp4
Ctrl
Dnmt3a
Trp53
AUC
1
0.8
0.6
0.4
0.2
0
B
-Log10(P value)
AUC
E2f1
C
E2f1
E2f2
E2f3
Ctrl
Dnmt3a
Trp53
Max
0
D
Shared
Vegfa
Zfp367
Slc6a
Camp
Rabgap1
Dck
...
E2F2
E2F3
E2F1
E
Zfp367
Slc6a
Camp
Rabgap1
Dck
WT
Trp53
Dnmt3a
E2F
H3K27me3
F
Log2 (OE efficiency)
0.00018
0.00027
Dnmt3a/Mock
Dnmt3a/E2f1
Trp53/Mock
Trp53/E2f1

Figure S11. Transcriptional basis for the pro-repairative phenotype of CH-mutant clones

A, Heat map showing activity of different regulons on a color scale among specific hematopoietic cell types.

B, Scatter plot showing the motif enrichment of each TF. AUC, area under curve.

C, UMAPs showing activity of the E2F regulons across all mutant vs. WT hematopoietic cells.

D, Logo plot showing the predicted motif enrichment in E2F1, E2F2, and E2F3. Selected genes were listed for the shared binding motif of E2F1, E2F2, and E2F3.

E, Genome browser tracks showing E2F and H3K27me3 binding signal at the loci of the listed genes predicted from (D) in mutant vs. WT macrophages.

F, Overexpression efficiency of E2F in *Trp53* or *Dnmt3a* mutant macrophages quantified by qRT-PCR and divided by non-infected *Trp53* or *Dnmt3a* mutant macrophages (n=3).